Atomistic insight into the defect-induced tunable plasticity and electronic properties of tetragonal zirconia

Sara Fazeli, Pascal Brault, Amaël Caillard, Anne-Lise Thomann, Eric Millon, Soumya Atmane, Christophe Coutanceau

To cite this version:

Sara Fazeli, Pascal Brault, Amaël Caillard, Anne-Lise Thomann, Eric Millon, et al.. Atomistic insight into the defect-induced tunable plasticity and electronic properties of tetragonal zirconia. Materials Today Communications, 2023, 36, pp.106731. 10.1016/j.mtcomm.2023.106731 . hal-04172270

HAL Id: hal-04172270
https://hal.science/hal-04172270v1

Submitted on 27 Jul 2023

Atomistic insight into the defect-induced tunable plasticity and electronic properties of tetragonal zirconia

Sara Fazeli[1*], Pascal Brault[1*], Amaël Caillard[1], Anne-Lise Thomann[1], Eric Millon[1], Soumya Atmane[1], Christophe Coutanceau[2]

[1] GREMI, Université d'Orléans / CNRS, 14 rue d'Issoudun BP6744, 45067 Orléans Cedex 2, France

[2] IC2MP, Université de Poitiers / CNRS, 4 rue Michel Brunet, 86022 Poitiers, France

Seyedehsara.fazeli@univ-orleans.fr ; Pascal.brault@ univ-orleans.fr

Abstract

Tetragonal zirconia (t-ZrO_2) with exceptional properties is crucial in catalytic applications. Defects effectively enhance its electronic properties and plasticity, making t-ZrO_2 a valuable material for high-efficiency industrial catalysts, and flexible electronic devices. In this study, we utilize first-principles calculations to compare the impact of vacancy defects and nitrogen doping on the structural and electronic properties of wide bandgap semiconductor t-ZrO_2. Additionally, we analyze the tuned plasticity of t-ZrO_2 by varying N-dopant and vacancy concentrations using molecular dynamics simulations and cyclic-nanoindentation tests. The estimation of energy release associated with plastic deformation is conducted using the Griffith energy balance model. Our study reveals significantly distinct electronic properties and plastic deformation maps in oxygen-deficient and N-doped t-ZrO_2 compared to the perfect counterpart, where the defect nature dictates the band gap energy and plastic zone size. t-ZrO_{2-x} exhibits a greater bandgap narrowing than t-$ZrO_{2-x}N_x$, resulting from increased atomic displacement, decreased free energy for plastic deformation, and enhanced plastic dissipated energy. Furthermore, we demonstrate that electronic properties and the plasticity of t-$ZrO_{2-x}N_x$, including bandgap energy and energy release rate during cyclic-nanoindentation, are unable to compete with those of the small-bandgap counterpart t-ZrO_{2-x}. Herein, t-ZrO_{2-x}, x=0.2 exhibits the highest plasticity and the smallest bandgap of 1.28 eV, contrasting with the 5.6 eV bandgap of perfect t-ZrO_2. Thereby, t-ZrO_{2-x} displays pronounced band gap tightening and enriched flexibility, providing it a favorable semiconductor for photoelectrochemical energy conversion (PEC) applications.

Keywords: tetragonal ZrO_2, defect, nanoindentation, bandgap, density functional theory, molecular dynamics simulation

1. Introduction

Providing clean, plentiful, and affordable energy is a vital policy and technical challenge for the 21st century[1-3]. As well as it is not possible to meet the universal energy requirements at the expense of climate and environmental deterioration. In this regard, scientists believe that finding novel energy resources to reduce dependence on fossil fuels must drive energy policy [4-6]. One of the promising strategies to overcome the lack of nonrenewable energy is to capture solar energy. This can be achieved by converting it to clean chemical energy through photo-electro-chemical energy conversion (PEC) systems [7-9]. Therefore, the development of a substitute and economically competitive approach to generate solar fuels is of strong interest. Furthermore, the development of novel materials and a thoughtful of defect processes in existing materials are required. Transition metal oxides [10-14] (TMOs) have been known as attractive candidates to provide high-performance[15], and low-cost [16] semiconductor materials for practical PEC solar fuel construction, owing to their outstanding mechanical [17] and electrical [18] properties. Among these promising TMOs, zirconia[19-20] (ZrO_2), one of the most important wide band-gap transition metal oxides [21], has attracted much attention owing to its exceptional properties such as high chemical durability[22], thermal stability[23], and high dielectric constant[24-25]. On the other hand, zirconia and zirconium oxynitride were considered as possible candidates for replacing platinum and more generally platinum group metal catalysts of proton exchange membrane fuel cells [26-27].

It has been known that the perfect t-ZrO_2 at atmospheric pressure shows three polymorphs: monoclinic phase ($P2_1/c$ space-group) below 1173°C, tetragonal phase ($P4_2/nmc$ space-group) from 1173 to 2370°C, and cubic phase (cubic fluorite, Fm3m space group) from 2370°C to the melting point (2680°C) [28-30]. However, the room-temperature phase of zirconia displays few applications. Instead, the tetragonal (t-ZrO_2) phase is recognized to possess interesting mechanical and reasonably catalytic properties. Nevertheless, a quite wide bandgap of ca. 5 eV [31] limits the t-ZrO_2 to be applied in high-efficiency catalytic applications [32]. Therefore, narrowing t-ZrO_2 bandgap is an interesting challenge. It has been demonstrated that defect engineering is an effective and facile strategy to achieve novel and particularly tunable band gaps [33]. In this regard, many efforts have been devoted to the study of crystalline materials based on perfect and defective zirconia both theoretically[34-36] and experimentally[21,37,38]. For instance, Khattab et al. [39], studied the effects of Nb and W dopants on the electronic and structural properties of monoclinic zirconia (*m*-ZrO_2), and they reported the band gap energy tightening from 5.79 eV to 0.89 eV and to 1.33 eV for m-ZrO_2:Nb and m-ZrO_2:W, respectively. Furthermore, it has been reported that the incorporation of defects, including oxygen vacancy [19,40], or the insertion of 2p light elements such as nitrogen[41-42] into the zirconia network opens up great opportunities for using stabilized zirconia in high-efficient electromechanical and catalytic systems.

Density functional theory (DFT) is a powerful technique to estimate the electronic density of states (DOS) and band structures of materials[43]. Tolba et *al*. [44]. studied the hydrogen dopant effect and oxygen shortage on the electronic properties of m-ZrO_2 by the DFT approach. They concluded that the size and concentration of defects directly affect the electronic properties of m-ZrO_2. Kiaser at *al.* [45] studied the band structure modifications of rhombohedral hafnium oxide in the presence of oxygen vacancies. Their DFT-based results showed that the oxygen vacancy induces midgap states in the rhombohedral phase and predicted a conducting defect band. Albanese et *al*. [42] employed DFT calculations based on B3LYP hybrid functional to examine the structural properties of N-dopants in m-ZrO_2 Bulk. They reported that the substitution of an O atom with N does not considerably influence the geometry, presenting insignificant changes in the local structure and the cell parameters. Nevertheless, most of the conducted research has focused on stabilizing [46] and controlling the size and shape [47] of defective zirconia. However, there has been little attention paid to the effect of oxygen vacancies and nitrogen dopants on atomic displacement [48] and deformation behavior [49]. The depth-sensing nanoindentation test is a popular way to probe the deformation behavior of a broad range of materials on an adequately small scale [50-53]. The nanoindentation load-depth (P–h) curve displays a series of yielding events, which are attributed to the movement of dislocations that can be connected to the mechanical and electronic properties[54-55]. It should be noted that the total energy consumed by plastic deformation and the stored elastic energy in materials is determined by calculating the area beneath a (P–h) curve[56]. A number of models can be implemented to quantitatively measure the energies during plastic deformation. Among them, the Griffith energy balance as a straightforward approach is presented to calculate the energy release rate (G_{in})[57]. Molecular dynamics (MD) simulations[58-60] have proven to be a prevailing tool for estimating the amount of G_{in} per unit of the deformed surface area during nanoindentation at the nanoscale. Zhong et *al.*[61] investigated the deformation behavior of single and polycrystalline crystals of yttria-stabilized zirconia by the MD-based nanoindentation simulations. Furthermore, Wang et *al.*[59] studied the deformation behavior of tetragonal zirconia under uniaxial tension by MD simulations. Their simulation results showed that the deformation mechanism of t-ZrO_2 is governed by phase transformation and intense dislocation activity, which directly influence electronic properties, as well as optical, mechanical, and catalytic behaviors.

In the present work, our main goals are: (i) Investigating the plastic deformation behavior and atomic displacement patterns of perfect t-ZrO_2, oxygen-deficient t-ZrO_{2-x}, and N-doped t-$ZrO_{2-x}N_x$ during cyclic-nanoindentation via MD simulations for varying defect concentrations. (ii) to provide fundamental insights on the differences in electronic properties of perfect t-ZrO_2 and defective t-ZrO_{2-x} and t-$ZrO_{2-x}N_x$ by DFT calculations, and (iii) to make a connection between the atomic displacement, plastic deformation, and electronic properties. This paper is organized as follows: We evaluate the electronic properties through DFT calculations in Section 2.1 and then describe the details of the MD simulation approach for modeling the cyclic nanoindentation in Section 2.2. Afterward, we provide a description of the structural and electronic properties of perfect and defective t-ZrO_{2-x}, and t-$ZrO_{2-x}N_x$ as a function of nature and concentration of defects by DFT study in Section 3.1. Then, we explain how the defect nature and concentration govern the load-depth curve, atomic displacements magnitude, plastic deformation maps, and the average plastic dissipation values during cyclic nanoindentation in Section 3.2. In addition, to obtain a full understanding of tuned plasticity in t-ZrO_2 subjected to cyclic nanoindentation, we quantitatively compare the energy release rate (G_{in}) and the free energy required for plastic deformation of t-ZrO_2, t-ZrO_{2-x}, and t-$ZrO_{2-x}N_x$ using the Griffith energy balance in Section 3.3. Finally, the main overall conclusions are summarized in Section 4. Therefore, our results provide guidance for the development of promising materials for industrial free-Pt catalysts, and photoelectrochemical energy conversion (PEC) applications.

2. Methodology

2.1. DFT Calculations

Density functional theory (DFT)[62] calculations are implemented using Quantum Espresso [63] with projected augmented wave (PAW)[64] potential to describe electronic band structures and the density of states (DOS). Amsterdam Modeling Suite (AMS) is used for running the simulations [65]. We modeled a 3×3×3 supercell of perfect t-ZrO_2 with dimensions X = 10.8Å, Y= 10.8Å, and Z = 15.51Å, as shown in the blue circle in Fig. 1. The 3×3×3 supercell of perfect t-ZrO_2 contains a total of 162 atoms comprising 54 Zr atoms and 108 O atoms. In addition, the Perdew-Burke-Ernzerhof (PBE) exchange-correlation functional within generalized gradient approximation (GGA)[66] is performed in all cases of the calculations. The kinetic energy cut-off is set to 816.33 eV for the plane wave basis set. Furthermore, the tolerance energy for the convergence is chosen as 0.01 meV to attain the self-consistency in the total energy. Optimizing all structures and calculating the electronic properties are performed using a Monhkorst-Pack grid of (4×4×4) k-points. The Hubbard approach was applied to avoid the underestimation error of DFT and precisely characterize the band gap energy. We set the Hubbard U parameters to 4.35 eV for 2p states of oxygen and nitrogen, and 8 eV for Zr 4d states, which are consistent with the Hubbard U parameters in ref. [39]

2.2. MD Simulations

All MD simulations are performed using an open-source Large – scale Atomic/Molecular Massively Parallel Simulator (LAMMPS)[67]. The third-generation charge-optimized many-body (COMB3)[68-69] potential was chosen to describe the forces among the atoms in the perfect and defective t-ZrO_2 structures, involving Zr-Zr, Zr-O, Zr-N, O-O, O-N, and N-N interatomic potentials. Before the nanoindentation test, the perfect t-ZrO_2 is first stabilized by performing constant number (N), volume (V), and temperature (T) (NVT) simulations on 14×14×9 unit cells at 300 K for 0.6 ns. Then we achieved oxygen-deficient ZrO_{2-x}, with x=0.1, x=0.14, and x=0.2 by introducing 6, 8, and 11 oxygen vacancies into the perfect t-ZrO_2 crystal, respectively. Additionally, introducing 6, 8, and 11 nitrogen dopants resulted in $ZrO_{2-x}N_x$ with x=0.1, x=0.14, and x=0.2, respectively. The defective structures were optimized at temperature for 600 ps. Free boundary condition (FBC) is employed in the Z direction, and periodic boundary conditions (PBC) are imposed in X and Y directions. Fig. 1 presents a three-dimensional model of the perfect t-ZrO_2 for the nanoindentation, which contains a diamond sphere indenter with a radius of 30 Å. The indenter was kept at a distance of about 5 Å over the surface. The substrate contains 24,000 atoms for the cases of perfect and t-$ZrO_{2-x}N_x$ samples, while the numbers of atoms in the cases of x= 0.1, 0.14, and 0.2 of OV-t-ZrO_2 are 23370, 23118 and 22740, respectively. The nanoindentation model is divided into the rigid layer, thermostat layer, and Newtonian layer as displayed in Fig. 1. The atoms in rigid layers were fixed for avoiding the substrate moving. The thermostat layers were maintained at a constant temperature of 300 K to restrict heat dissipation, using a Nosé-Hoover scheme. The motion of the Newtonian atoms is free and followed classical Newton's second law. The equations of motion were integrated with the velocity-Verlet algorithm with a time step of 0.1 fs. A constant loading and unloading rate of 5.0 ms^{-1} was employed during the whole cyclic nanoindentation test. The maximum penetration depth in all simulation samples was set at 30 Å for each cycle. Each cycle was completed for 800 ps, corresponding to a total simulation time of 2400 ps. The applied force during nanoindentation on atoms can be described by the F(r) = −K(r-R) ^{2} equation, where K denotes the force constant and is set to 10 eV Å^{-3}. Also, r and R are the distance from the atom to the axis of the indenter, and the radius of the indenter, respectively. The force is considered repulsive and can be set as zero for r > R.

$$F = \begin{cases} -K\,(r-R)^2\,, & r < R \\ 0\,, & r \geq R \end{cases} \tag{1}$$

Free software OVITO[70] was used to visualize the MD results.

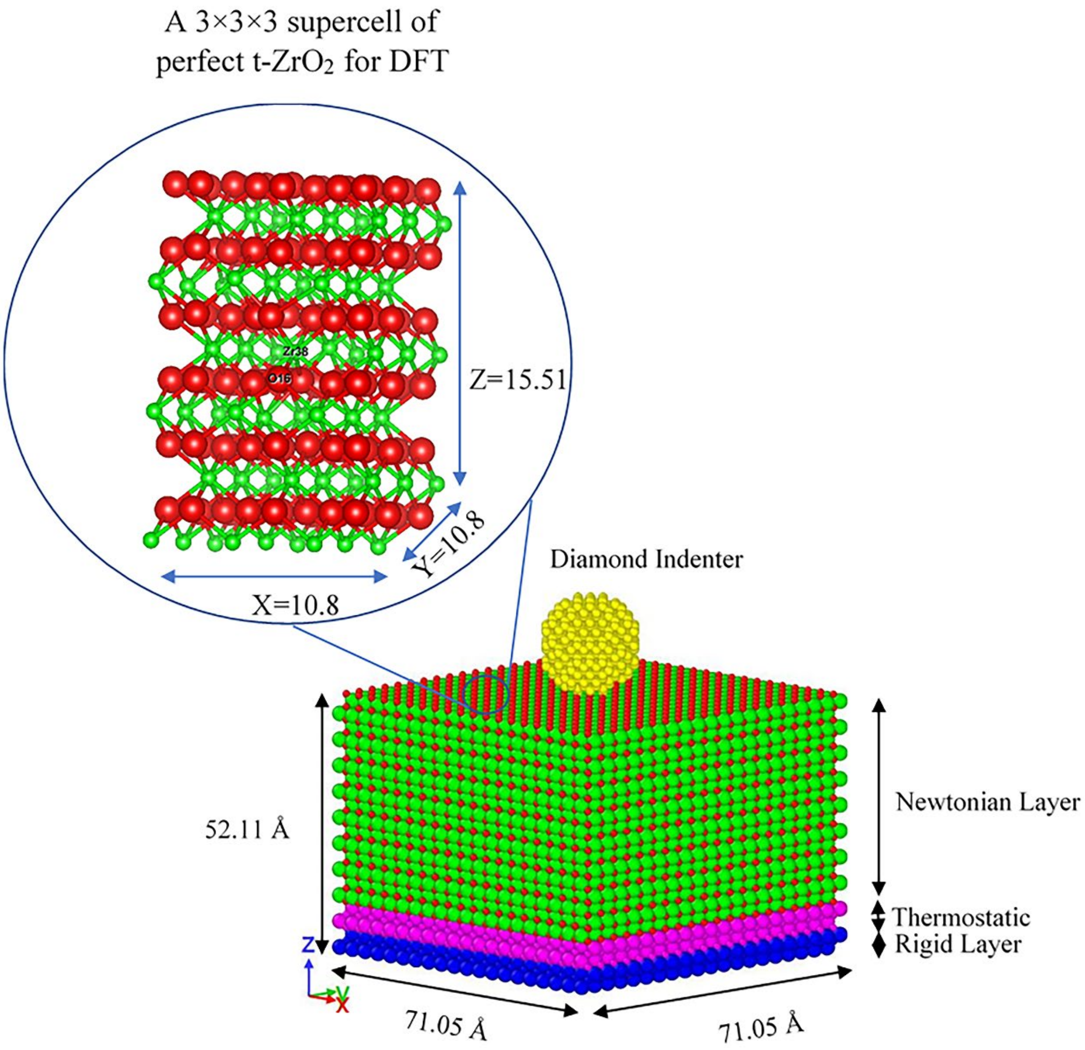

Fig. 1 Three-dimensional MD simulation model of the perfect t-ZrO_2 for cyclic-nanoindentation test. Green and red represents Zr and O atoms of t-ZrO_2, respectively.

3. Results and discussions

3.1. DFT Calculations

3.1.1. Structure

Defect incorporation in t-ZrO_2 is expected to influence the electronic structures of the solid. For instance, oxygen vacancies can be considered as intrinsic defects of metal oxides with paramount importance in various applications such as photoelectrocatalysis. Moreover, the substitution of oxygen atoms in t-ZrO_2 phase by dopants, such as nitrogen atoms probably plays an essential role in its characteristic redox properties[71]. In this section, the change in the electronic properties of t-ZrO_2 caused by different concentrations of oxygen vacancy and nitrogen dopant at random positions is investigated by DFT calculations. Before starting to discuss the electronic modification due to the punctual defects, we briefly describe the crystal structure of the perfect and defective t-ZrO_2. The structure of the perfect t-ZrO_2 crystal has a $P4_2/nmc$ space group with unit cell parameters of a= b=3.6055 Å and c=5.1797Å [72]. In this structure, assuming an ionic bond between Zr and O species, and each Zr^{4+} ions is bonded to eight equivalent O^{2-} ions in a distorted body-centered cubic geometry. According to Fig. 2, eight Zr-O bonds are observed, with four of them (Zr-O_2, Zr-O_3, Zr-O_6, and Zr-O_7) measuring 2.39 Å in length and the other four (Zr-O_1, Zr-O_4, Zr-O_5, and Zr-O_8) measuring 2.08 Å.

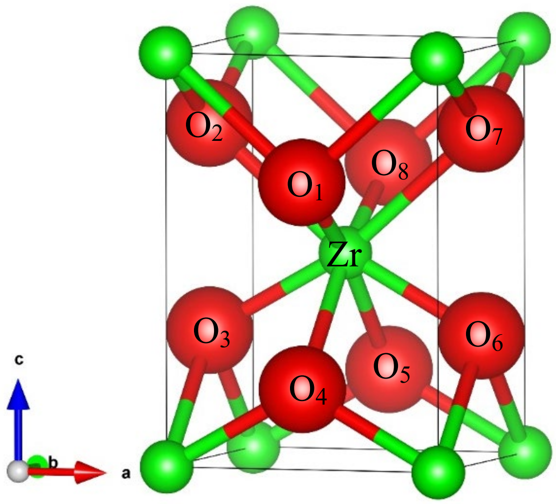

Fig. 2. structural details of a unit cell of perfect-t-ZrO_2.

To assess the influence of oxygen vacancies or nitrogen dopant, we modeled a 3×3×3 supercell of t-ZrO_2, selected 6, 8, and 11 oxygen ions, and then randomly removed them to build defective t-ZrO_{2-x}. Once again, we replaced 6, 8, and 11 of oxygen ions with nitrogen ions to create t-$ZrO_{2-x}N_x$. Mulliken population analysis is widely used to examine the charges of atomic systems and electronic populations. The average Mulliken charges on O and Zr ions of the optimized structures of perfect t-ZrO_2, t-ZrO_{2-x}, and t-$ZrO_{2-x}N_x$ are tabulated in Table 1. For perfect t-ZrO_2, the average Mulliken charges on Zr and O ions are +3.39 and -1.69, respectively. For t-ZrO_{2-x}, x=0.1, the average charge values on Zr and O ions are +3.18 and -1.68, respectively, while for the t-$ZrO_{2-x}N_x$, x=0.1, the average Mulliken charges are 3.35, -1.67, and -1.71 for Zr, O, and N ions, respectively. These results demonstrate that the distribution of positive charges on Zr ions and negative charges on O ions varies in response to the type and concentration of defects. The Mulliken charges decrease and increase on Zr and O ions nearby the vacancies of t-ZrO_{2-x}, respectively. Nevertheless, there is a little difference in the magnitude of charges on both Zr and

O ions throughout the entire structure. Furthermore, the introduction of N dopants considerably changes the Mulliken charges on both Zr and O ions adjacent the defect. However, the Mulliken charges on ions located far from the N-dopant exhibit only mirror modifications.

Table 1. Average Mulliken charges of perfect t-ZrO2, t-ZrO_{2-x}, and t-$ZrO_{2-x}N_x$.

		Average Mulliken Charge
Perfect-t-ZrO_2	O	-1.69
	Zr	+3.39
t-ZrO_{2-x}, x= 0.1	O	-1.68
	Zr	+3.18
t-ZrO_{2-x}, x= 0.14	O	-1.68
	Zr	+3.11
t-ZrO_{2-x}, x= 0.2	O	-1.67
	Zr	+3.10
t-$ZrO_{2-x}N_x$, x= 0.1	O	-1.67
	Zr	+3.35
	N	-1.71
t-$ZrO_{2-x}N_x$, x= 0.14	O	-1.66
	Zr	+3.34
	N	-1.71
t-$ZrO_{2-x}N_x$, x= 0.2	O	-1.66
	Zr	+3.33
	N	-1.70

We analyze the rearrangement and the magnitude of atomic displacement due to the insertion of O-vacancy or N-dopants into the crystal. The schematics of the magnitude of atom displacements and corresponding optimized structures of t-ZrO_{2-x}, x=0.1, and t-$ZrO_{2-x}N_x$, x=0.1 are illustrated in Figs. 3a-3d. The oxygen vacancy sites are presented as the dashed purple circle. In addition, N-dopant is indicated by the blue color (Fig. 3d). The changes in the coordination of atoms are shown by arrows. Interestingly, the creation of O-vacancies induces long-range rearrangement that leads to relatively uniform Mulliken charge distribution throughout the defective structure, thereby compensating for the charge. While all oxygen atoms cause disruption in the crystalline structure, those located adjacent to the initial O-vacancy site exhibit greater displacement towards the vacancy (Fig. 3a). This is reflected in a slightly larger decrease and increase of Mulliken charges on Zr and O ions around the vacancy. Fig. S1 in the supplementary information shows the magnitude of atom displacements in the other structures, which contain x=0.14 and x=0.2 defects. At different defect concentrations, t-ZrO_{2-x} and t-$ZrO_{2-x}N_x$ exhibit distinct rearrangements and magnitudes of atomic displacement, as depicted in Fig. 3 and Fig. S1.

Fig. S1a indicates that for x=0.14, t-ZrO_{2-x} exhibits greater rearrangement of O atoms near the vacancy site than for x=0.1. Subsequently, the greatest rearrangement of O atoms near the defect site is observed in t-ZrO_{2-x} for x=0.2 (Fig. S1b). Importantly, these results are consistent with the magnitude of atomic displacements obtained by MD simulations (See section 3.2.2.). On the contrary, the substitution of O ions with N ions at different concentrations would not alter considerably the geometry and will display insignificant disarrangement in the local structure. On one hand, it can be seen in Fig. 3c that the substitution of O ions by N ions leads to a short-range rearrangement around the defect with the spontaneous creation of N—O bonds with three electrons localized in the π antibonding orbitals, as reported in ref [42]. On the other hand, as nitrogen is introduced into the crystal, the bond N-Zr length nearby the N-doped site shortens, and simultaneously a new O-N bond can be created (Fig. 3d). The Mulliken charge values in defect region of t-$ZrO_{2-x}N_x$, x=0.1 contains N_6, O_{92} and Zr_{12} ions are -1.32, -1.24 and 3.19, respectively. Additionally, O and Zr ions located far from the N-doped region have Mulliken charge values of -1.69 and 3.36, respectively. This suggests that the Mulliken charges of a small defect region are affected by N-dopant. Zr atoms nearby the N-dopant possess the minimum displacement magnitude owing to the formation of the new N—O bond (Fig. 3c).

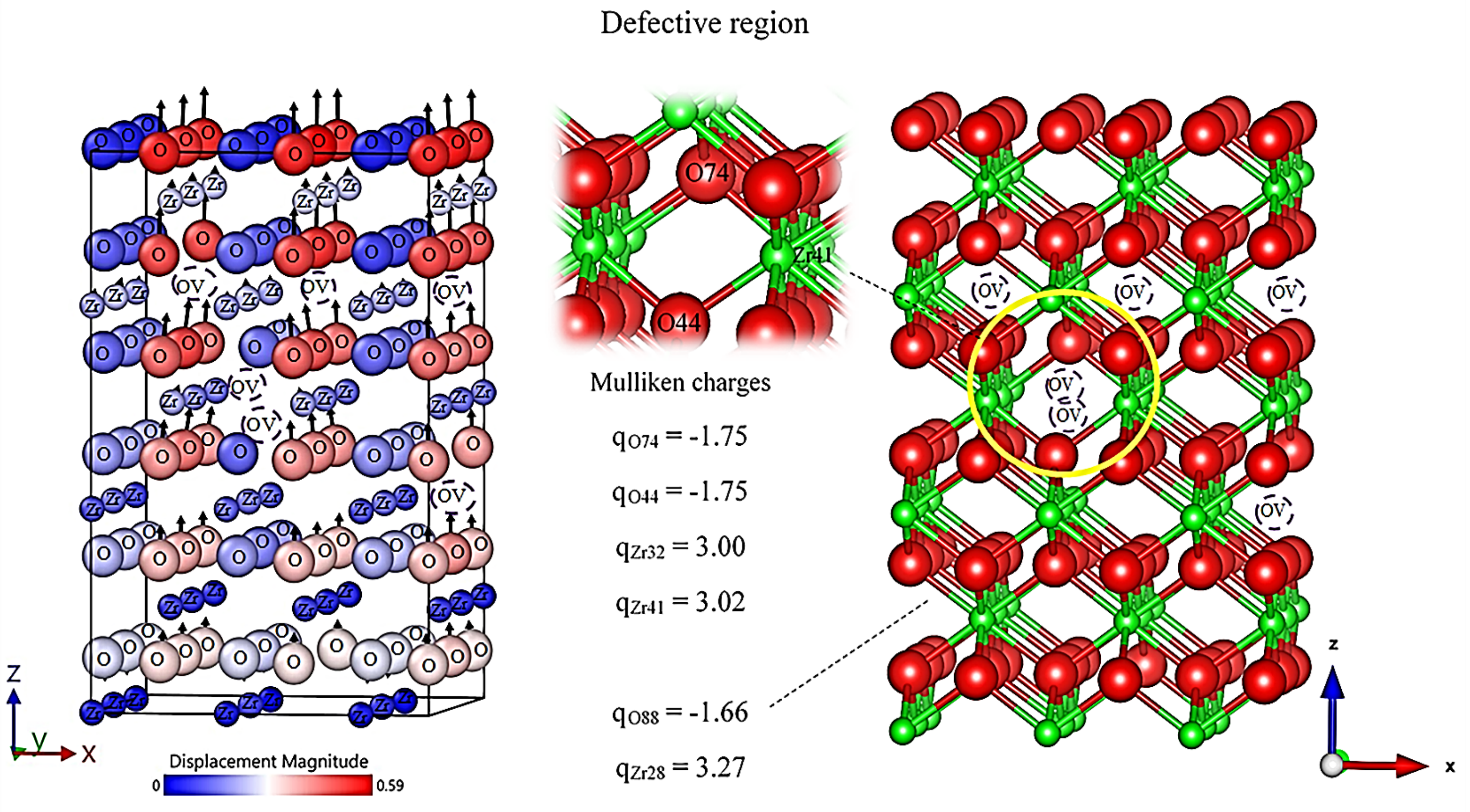
Defective region
Displacement Magnitude
0
0.59
OV
O74
O44
Zr41
Mulliken charges
q_{O74} = -1.75
q_{O44} = -1.75
q_{Zr32} = 3.00
q_{Zr41} = 3.02
q_{O88} = -1.66
q_{Zr28} = 3.27
z
y
x

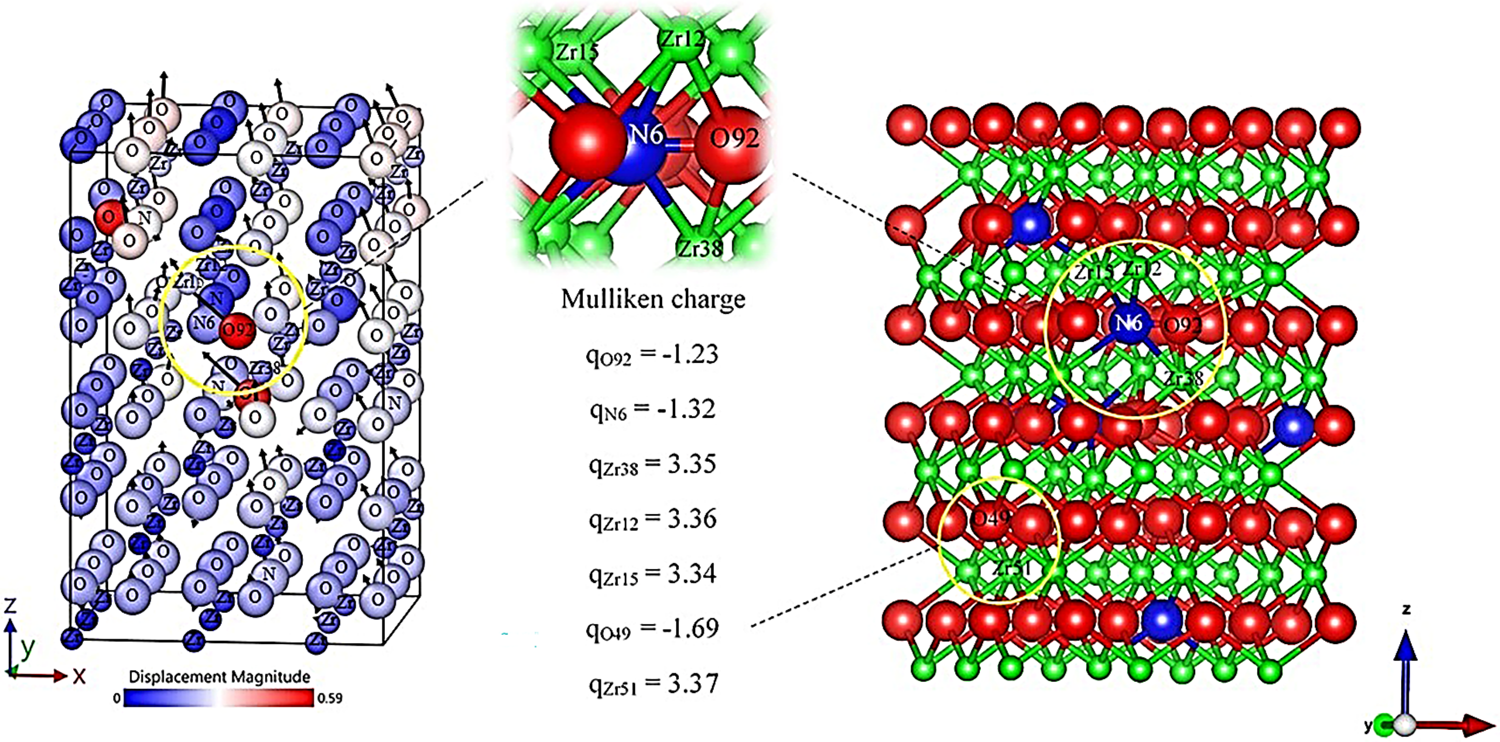
Zr15
Zr12
N6
O92
Zr38
Mulliken charge
q_{O92} = -1.23
q_{N6} = -1.32
q_{Zr38} = 3.35
q_{Zr12} = 3.36
q_{Zr15} = 3.34
q_{O49} = -1.69
q_{Zr51} = 3.37
O49
Zr51
Displacement Magnitude
0
0.59
z
y
x

(c)

(d)

Fig. 3. (a) Magnitude of atom displacement of t-ZrO_{2-x}, x=0.1, (b) atomic structure of optimized t-ZrO_{2-x}, x=0.1, (c) magnitude of atom displacement of t-$ZrO_{2-x}N_x$, x=0.1, (d) atomic structural of optimized t-$ZrO_{2-x}N_x$, x=0.1. The sites of the oxygen vacancy are presented as the dashed purple circle (a,b). N-dopant is indicated by the blue color (c,d). Arrows indicate the changes in the coordination of atoms.

3.1.2 Effect of oxygen vacancy and N-dopant on the electronic properties of t-ZrO_2

Investigating the local structure of t-ZrO_2 at varying defect concentrations offers crucial theoretical insights into how the electronic properties depend on the nature and concentration of defects. Detailed analysis of band structures and density of states (DOS) throws light on the electronic properties of defects. Fig. 4 displays the electronic band structures and DOS plot of the perfect t-ZrO_2. The perfect t-ZrO_2 shows a bandgap of 5.6 eV, in excellent agreement with the experimental ones (5-6 eV)[31]. As can be seen from the DOS plot, the O (2p) and Zr (4d) electronic states prevail in the valence band maximum (VBM) and the conduction band minimum (CBM), respectively.

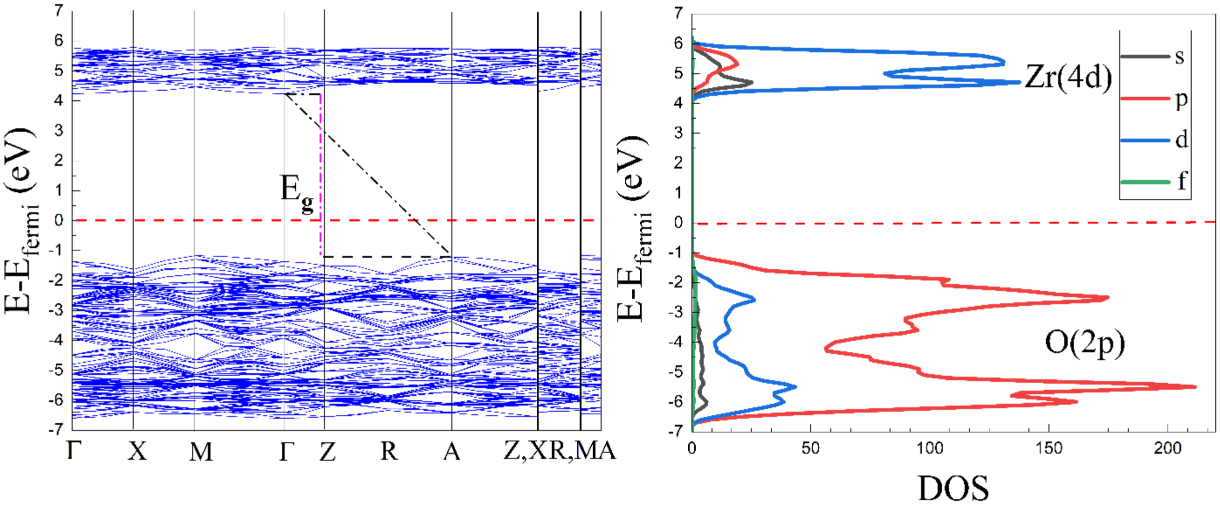

Fig. 4. Band structure and DOS of perfect t-ZrO_2

In addition, the band structures and DOS of t-ZrO_{2-x}, x=0.1, and t-$ZrO_{2-x}N_x$, x=0.1 are illustrated in Fig. 5a and Fig. 5b, respectively. Details of electronic structures at the defect concentrations of x=0.14 and x=0.2 are drawn in Fig. S2. Table 2 provides the deduced band gap values of the perfect t-ZrO_2, t-ZrO_{2-x}, and t-$ZrO_{2-x}N_x$. The results of Table 2 reveal that in the case of oxygen-deficient t-ZrO_2, the introduction of OV decreases the bandgap value of perfect t-ZrO_2 from 5.6 eV at x = 0 to 2.5 eV at x = 0.1. In addition, as OV concentration increases from x=0.1 to x=0.14, and x=0.2, the bandgap energy of t-ZrO_{2-x} decreases from 2.5 eV to 1.32 eV and 1.28 eV, respectively. This is in line with what can be detected in the literature[73] for other defective metal oxides. Also, a similar trend is observed for band gap energy in t-$ZrO_{2-x}N_x$ with different concentrations of N-dopant. Band gap energy values of 3.74 eV, 3.63 eV, and 3.49 eV were obtained for x= 0.1, x = 0.14, and x = 0.2 of N-dopants, respectively. These values correspond to a reduction of 33.68%, 34.62%, and 35.37% compared to the bandgap energy of perfect t-ZrO_2.

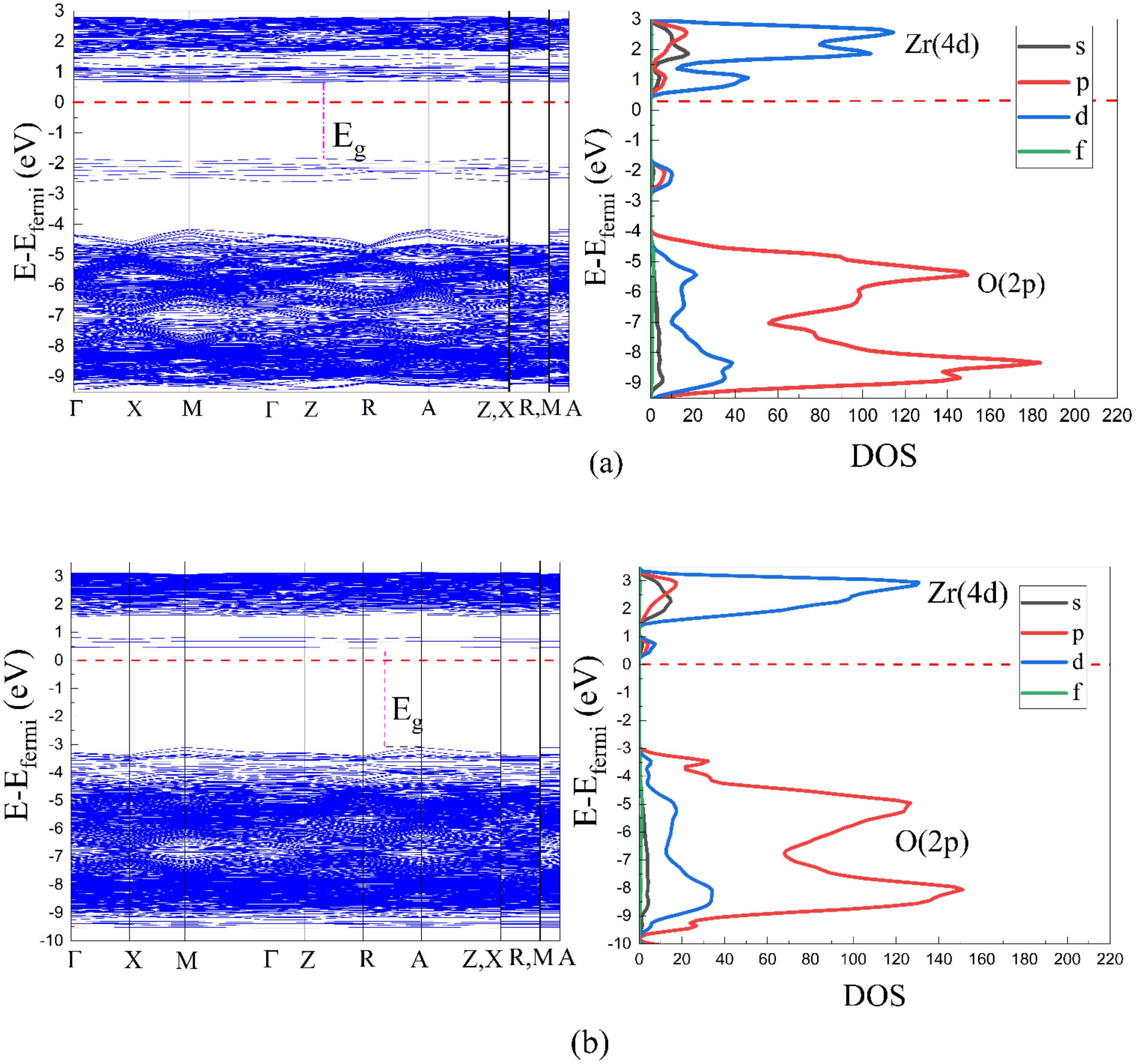

Fig. 5. Band structure and DOS of defective (a) t- ZrO_{2-x}, x=0.1, (b) t- $ZrO_{2-x}N_x$, x=0.1

Table 2. The calculated bandgap energy of perfect t-ZrO_2 and t-ZrO_{2-x}, and t-$ZrO_{2-x}N_x$, x=0.1, 0.14, and 0.2.

	Bandgap Energy (eV)
Perfect t-ZrO_2	5.6 (5-6 eV of exp[31])
ZrO_{2-x},x = 0.1	2.50
ZrO_{2-x},x = 0.14	1.32
ZrO_{2-x},x = 0.2	1.28
$ZrO_{2-x}N_x$, x = 0.1	3.74
$ZrO_{2-x}N_x$, x = 0.14	3.53
$ZrO_{2-x}N_x$, x = 0.2	3.49 (3.43 eV of exp [71])

As shown in DOS plots of defective t-ZrO_2 (Fig. 5, and Fig. S2), the nature and concentration of defects influence clearly the hybridization of oxygen (2p) and zirconium (4d) orbitals. The valence band in all cases mainly comprises O (2p) bonding states, with a minor contribution from Zr (4d) states. Moreover, the conduction band minimum (CBM) is mostly comprised of the (4d) states of Zr. Consequently, the reduction of the band gap value for t-ZrO_{2-x} and t-$ZrO_{2-x}N_x$ crystals (Table 2) is explained by the incorporation of 4d orbitals of Zr and 2p orbitals of N atoms (in the cases of t-$ZrO_{2-x}N_x$) or by the remaining of two electrons in the vacancy (in the case of t-ZrO_{2-x}). Fig. 5a demonstrates significant edge position modifications in t-ZrO_{2-x}, x=0.1 compared to perfect t-ZrO_2, indicating alterations in the local environment and the density of unoccupied electronic states near vacancies. In addition, The edge positions (CBM or VBM) move to lower energies with the increase of the OV concentration (Fig. 2Sb, and Fig. 2Sc). It means that for t-ZrO_{2-x} with x=0.1, 0.14, and 0.2, the CMB position decreases, representing 82.5%, 83.5%, and 85.2% of the CBM value of perfect t-ZrO_2, respectively. Reduction of the CBM level allows electrons to reach quickly the conduction band and subsequently decreases the band gap. Increasing the OV concentration, results in a narrowing of the bandgap and the emergence of more prominent peaks, attributed to the hybridized contribution of oxygen (2p) and zirconium (4d) orbitals, and emergence of energy levels in the middle of the band gap. These levels are occupied by localized electrons situated at the oxygen vacancy sites [74].Indeed, oxygen vacancy defects leave two electrons in the system. So, the additional defect electrons are captured through the vacancy-induced states, which lie within the t-ZrO_2 bandgap. According to Fig. 5a, six occupied levels above the top of the valence band at -2.6 eV have been identified in the case of t-ZrO_{2-x}, x=0.1. The additional elimination of oxygen ions from the perfect structure (introducing x=0.14, and x=0.2 of OV) leads to more occupied levels in the bandgap (Fig. S2a- Fig. S2b). The removal of oxygen ions creates dangling bonds on the adjacent Zr ions. Therefore, the defect orbital can be highly localized at the two Zr neighbors.

Fig. 5b and Figs. 2Sc-2Sd indicate a minor difference in the height and edge position of the midgap band related to the t- $ZrO_{2-x}N_x$ phases at different N-dopant concentrations. It is shown that the top of the valence bands (VBM) of t-$ZrO_{2-x}N_x$ with x=0.1 and 0.14, and 0.2 are shifted to values of ca. -2eV lower than that of the perfect t-ZrO_2. Narrowing the band-gap by increasing the N-dopant contents is related to introduce additional deep-acceptor energy levels in the band-gap, near the conduction and valence bands, as depicted in Fig. 5b and Figs. 2Sc-2Sd. Furthermore, the energy ranges from ca. -3 eV to ca. 1.8 eV involve hybridized-deeper valence states for t-$ZrO_{2-x}N_x$ with different N-dopant concentrations. Multiple occupied states are formed by nitrogen (2p) orbitals, which appear ca. 0.5 eV below the conduction band of t- $ZrO_{2-x}N_x$. This demonstrates that the density of states (DOS) of t-$ZrO_{2-x}N_x$ narrows as the N-dopant concentration increases, albeit not at a significant rate. On the other hand, the DOS of t- $ZrO_{2-x}N_x$ is influenced by the short-range displacement of atoms, which is consistent in the discussion of section 3.1.1. On the other hand, this modification in the band gap energy can be connected to the covalent bond character between oxygen and nitrogen ions, reducing the strong electronegativity of oxygen ions in O–Zr ionic bonds (See Fig. 3d).

Table 2 provides evidence that t-ZrO_{2-x} exhibits a significantly lower band gap value compared to t-$ZrO_{2-x}N_x$, regardless of the concentration of defects. The spectra of t-ZrO_{2-x} (Fig. 5a, Figs. 2Sa-2Sb) show major changes with increasing oxygen vacancy (OV) content, while the spectra of t-$ZrO_{2-x}N_x$ display only minor changes (Fig. 5b, Figs. 2Sc-2Sd). Specifically, the differences in band gap energies among different concentrations of t-$ZrO_{2-x}N_x$ are smaller than 0.5 eV. The underlying reason for these observations can be explained as follows: oxygen vacancies induce greater atomic displacement at longer distances, leading to a shift of adjacent oxygen ions towards the vacancy site. This displacement results in the formation of diverse Zr dangling bonds, creating defect states. Conversely, the limitation of atomic displacement in t- $ZrO_{2-x}N_x$ can be attributed to the presence of inter-layer nitrogen bridges, which restrict the movement of atoms. Consequently, the main atomic displacement primarily involves oxygen ions. It is worth noting that this reconstruction has the potential to spread to neighboring layers, as discussed in Section 3.1.1. Hence, even with a further increase in the concentration of nitrogen dopants, the band gap energy exhibits minimal changes.

3.2 MD simulations

3.2.1 Load-displacement curves of perfect-t-ZrO_2

This section presents the results of numerical cyclic nanoindentation tests, offering insights into the influence of defect nature and concentration on the deformation behavior of t-ZrO_2. The analysis quantifies parameters such as average plastic energy dissipation per unit ($E_{plastic}$), energy release rate (G_{in}), and the free energy required for plastic deformation.

Results for the load as a function of indentation depth (*P-h* curve) for the perfect t-ZrO_2 are shown in Fig. 6. The upward and downward arrows in nanoindentation curves represent the loading and unloading processes. To clarify the deformation behavior of the perfect t-ZrO_2 versus depth, we indicate the chosen points I (h = 9.5Å), II (h =17.8 Å), III (h = 22.3 Å), and IV (h_{max} = 30 Å) in Fig 6. The structural evaluation of perfect-t-ZrO_2, specifically from point (I) to point (IV), showcasing the plastic deformation behavior under the indentation load based on atom displacement magnitude are illustrated in Fig. 6. These snapshots display how the stress-induced deformation response changes with increasing the indentation depth. As can be seen from Fig. 6, two distinguished deformation regimes are identified in the *P-h* curve. For h < ca. 9.5Å, the slightly linear responses of load-depth curves denote the elastic deformation. After the elastic stage, a steep load drop in the *P-h* curve occurs, which corresponds to the beginning of the elastic-to-plastic transition. It can be considered a pop-in event. As evidenced in point (I), the first pop-in event happens in the indentation depth of ~ 9.5Å. Minor fluctuations, corresponding to increased atom displacement and higher magnitudes of displacement under indentation load, along with transitions from elastic to plastic deformation, are observed for h values ranging between 9.5Å and 17.8Å.

In the range 17.8Å ≤ h ≤ 22.3 Å, the *P-h* curve fluctuates strongly and displays a zigzag shape. This behavior is attributed to plasticity growth[59]. As the depth increases (22.3Å ≤ h ≤ 30 Å), more atoms are involved in plastic deformation.

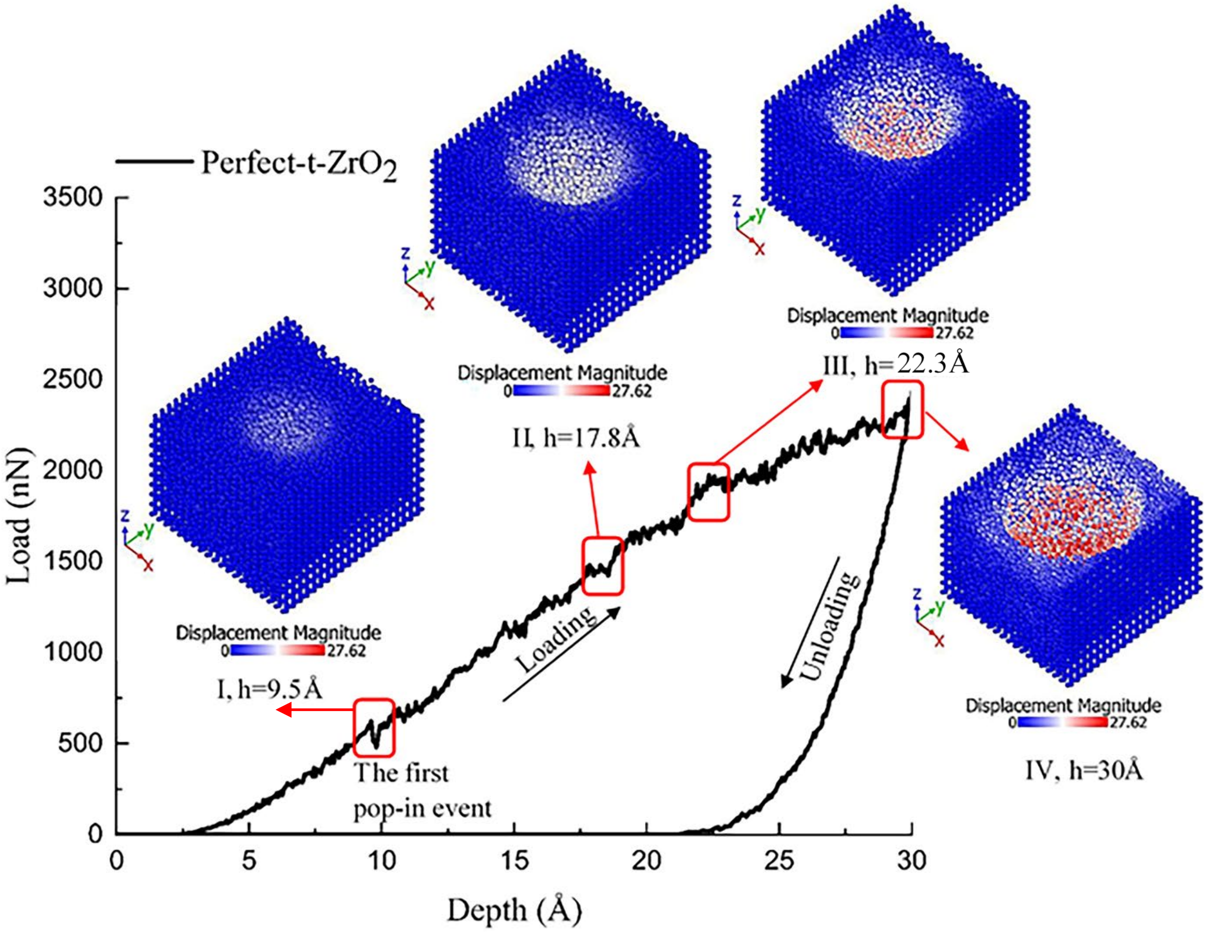

Fig. 6. Indentation load-depth curve of perfect t-ZrO$_2$, and structural evaluation of the perfect t-ZrO$_2$ structure under the sphere indenter at different indentation depths.

3.2.2 Indentation-induced plastic deformation of t-ZrO_{2-x} and t-$ZrO_{2-x}N_x$

Fig. 7a represents the comparative analysis of the load-depth curves of t-ZrO_{2-x} at three levels of defect concentrations. The *P-h* curves of t-$ZrO_{2-x}N_x$, x=0.1, 0.14, and 0.2 are given in Fig. 7b. Both elastic and plastic evident stages are observed in Fig. 7a and Fig. 7b, as well as fluctuations with different intensities. The first pop-in events happen in the indentation depth of ca.11.5 Å, ca. 6.9Å, and ca. 6.2Å in $ZrO_{2-x,}$ x=0.1, $ZrO_{2-x,}$ x=0.14, and $ZrO_{2-x,}$ x=0.2, respectively (Fig. 7a). Also, the first pop-in events appear at ca. 14.0Å, ca. 11.2 Å, and ca. 14.15 Å in t-$ZrO_{2-x}N_{x,}$ x=0.1, t-$ZrO_{2-x}N_{x,}$ x=0.14, and t-$ZrO_{2-x}N_{x,}$ x=0.2, respectively (Fig. 7b). It is well understood from Fig. 7a that the deformation response of t-ZrO_{2-x} is significantly influenced by defect concentration. As the OV concentration increases the fluctuations of the indentation load of ZrO_{2-x} intensified. Hence, complex deformation behavior is expected in t-ZrO_{2-x}, x=0.2 during the plastic stage. On the contrary, when the N-dopant of the crystal is performed with different concentrations, the nanoindentation load-depth curves are not considerably disrupted. Therefore, there is no notable difference in pop-in events of t-$ZrO_{2-x}N_x$ at different concentrations of N-dopant (Fig. 7b).

To examine the effect of OV or N-dopant defects on the stress-induced plastic deformation of t-ZrO_2, cyclic nanoindentation simulations were used to calculate plastic energy dissipation ($E_{plastic}$). $E_{plastic}$ is the result of permanent deformation in which energy can be transformed from one form to another one. The non-nonlinear response, pop-in events, and the intensified fluctuation of the load-depth curve can be quantified as plastic energy dissipation ($E_{plastic}$).

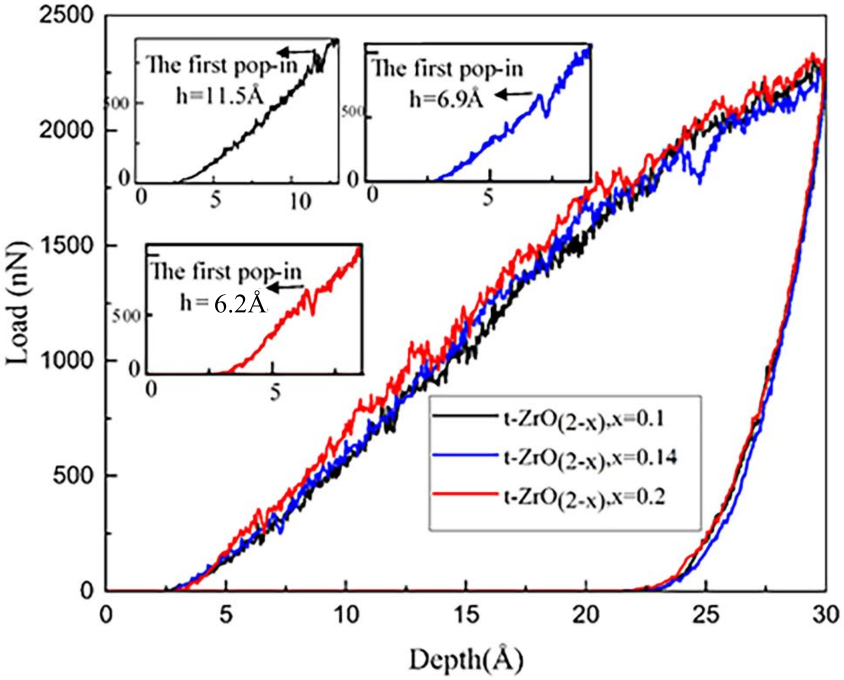

The first pop-in
h=11.5Å
The first pop-in
h=6.9Å
The first pop-in
h= 6.2Å
t-ZrO(2-x),x=0.1
t-ZrO(2-x),x=0.14
t-ZrO(2-x),x=0.2
Load (nN)
Depth(Å)
0
500
1000
1500
2000
2500
0
5
10
15
20
25
30

(a)

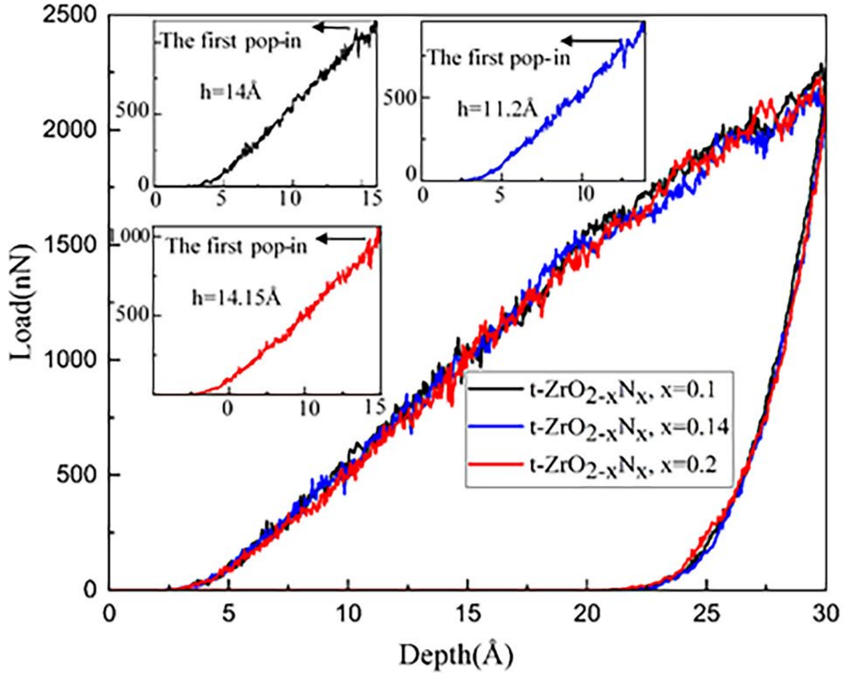

The first pop-in
h=14Å
The first pop-in
h=11.2Å
The first pop-in
h=14.15Å
t-ZrO2-xNx, x=0.1
t-ZrO2-xNx, x=0.14
t-ZrO2-xNx, x=0.2
Load(nN)
Depth(Å)
0
500
1000
1500
2000
2500
0
5
10
15
20
25
30

(b)

Fig. 7 Comparative nanoindentation load-depth curves of (a) t-ZrO_{2-x}, x= 0.1, 0.14, and 0.2, (b) t-$ZrO_{2-x}N_x$, x= 0.1, 0.14, and 0.2

The ($E_{plastic}$) value can be calculated for each cycle according to eq 2[75]:

$$E_{plastic} = E_{loading} - E_{unloading} = \int_{loading} Fd\delta - \int_{unloading} Fd\delta \qquad (2)$$

Where $E_{loading}$ and $E_{unloading}$ are the integrated values of the loading and unloading forces with respect to indentation depth during the loading and unloading process of cyclic nanoindentation tests, respectively.

Subsequently, the average plastic energy dissipated in the cyclic nanoindentation is considered as:

$$E_{plastic} = \frac{1}{n_{max}} \sum_{n=1}^{n_{max}} E_{plastic}^{max} \qquad (3)$$

Where n_{max} is the maximum number of indentation cycles performed in the cyclic nanoindentation test. In this study, the maximum number of cycles is set to three. Cyclic load-depth curves of the perfect and defective t-ZrO_{2-x} and t-$ZrO_{2-x}N_x$ are reported in Fig. S3. In addition, the values of the $E_{plastic}$ for the perfect and defective structures with different concentrations of OV and N-dopant, for the same penetration depth are listed in Table 3. According to the obtained results, the $E_{plastic}$ of perfect t-ZrO_2 (106.80 nJ) is lower than those of t-ZrO_{2-x} and t-$ZrO_{2-x}N_x$. It is essential to note that the higher value of $E_{plastic}$ should be linked to more permanent plastic deformation in the deformed zone resulting from the cyclic nanoindentation. In addition, it is demonstrated that $E_{plastic}$ values of t-$ZrO_{2-x}N_x$ are lower than those of t-ZrO_{2-x} for the same defect concentrations. Besides, the $E_{plastic}$ value increases with increasing the defect concentrations in both defective structures. For the same defect concentration, the value of $E_{plastic}$ for t-ZrO_{2-x}, x=0.2 (ca. 129.34 nJ) and t-

$ZrO_{2-x}N_x$, x=0.2 (ca. 109.21nJ) have increased to ca. 14.38% and ca. 2.25% compared to perfect t-ZrO_2. (ca. 106.80 nJ), respectively (Table 3). It means that the probability of permanent plastic deformation occurrence for t-ZrO_{2-x} is almost 1.18 times higher than that for t-$ZrO_{2-x}N_x$. It is important to note that, the increases of ca. 3.63% and ca. 8.98% of $E_{plastic}$ value are observed by increasing the OV concentration to x=0.14 and x=0.2, respectively, in comparison with t-ZrO_{2-x}, x=0.1. Only ca. 0.78% and ca. 2.00% increases in $E_{plastic}$ are estimated by increasing the N-dopant concentration to x=0.14 and x=0.2, respectively, in comparison with t-$ZrO_{2-x}N_x$, x=0.1. Increasing the concentrations of N-dopant in t-ZrO_2 does not significantly impact the deformation mechanism, unlike the notable effect observed with increasing concentrations of OV.

Table 3. E_{plastic} values obtained for the perfect t-ZrO_2 and t-ZrO_{2-x}, t-$ZrO_{2-x}N_x$, with x= 0.1, 0.14, and 0.2.

	$E_{plastic}$ (nJ)
Perfect t-ZrO_2	107
t-ZrO_{2-x}, x=0.1	118
t-ZrO_{2-x}, x=0.14	122
t-ZrO_{2-x}, x=0.2	129
t-$ZrO_{2-x}N_x$, x=0.1	107
t-$ZrO_{2-x}N_x$, x=0.14	108
t-$ZrO_{2-x}N_x$, x=0.2	109

Comparing atom displacement magnitudes under external loading reveals plastic deformation differences between perfect and defective t-ZrO_2 at maximum indentation depth. It is now generally recognized that atom displacements are induced during plastic deformation and influence the mechanical and electronic properties. It is also noted that a small value of atomic displacement is consistent with small plastic deformation, and subsequently small changes in electronic properties. Fig. 8a presents a comparison of atomic displacement distributions along the z direction for perfect t-ZrO_2 and t-ZrO_{2-x} at various defect concentrations beneath the indenter. Similarly, Fig. 8b demonstrates the corresponding results for t-$ZrO_{2-x}N_x$. As can be understood from Fig. 8, the defect nature and concentration have different effects on the deformation behavior of t-ZrO_2. First, the magnitude of atom displacement for the perfect t-ZrO_2 at the maximum indentation depth is smaller than those for defective t-ZrO_{2-x}, and t-$ZrO_{2-x}N_x$. Second, compared to t-$ZrO_{2-x}N_x$ structures, t-ZrO_{2-x} samples experience more atom displacements. Third, the magnitude of the indentation-induced atom displacement along the z direction decreases in the order of t-ZrO_{2-x}, x=0.2 > t-ZrO_{2-x}, x=0.14 > t-ZrO_{2-x}, x=0.1 > t-$ZrO_{2-x}N_x$, x=0.2 > t-$ZrO_{2-x}N_x$, x=0.14 > t-$ZrO_{2-x}N_x$, x=0.1 > perfect-t-ZrO_2. In order to gain a better understanding of the influence of defects on the atomic displacement pattern in t-ZrO_2, we provide a comparison of shear strain colored deformation maps at the maximum indentation depth. The comparison includes perfect t-ZrO_2, t-ZrO_{2-x}, x=0.2, and t-$ZrO_{2-x}N_x$, x=0.2, as depicted in Figs. 8c and 8b. The plastic flow clearly emerges in the plastic deformation zone as shown with the black arrows (Figs. 8c and 8b). Interestingly, both defective t-ZrO_2 samples exhibit a greater abundance of atoms with higher shear strain (indicated by the red color) in the plastic deformation region compared to the perfect counterpart. Additionally, noticeable differences in atomic displacement magnitudes and the existence of atoms with higher shear strain are witnessed during the indentation process of t-$ZrO_{2-x}N_x$, x=0.2 and t-ZrO_{2-x}, x=0.2. The sample of t-$ZrO_{2-x}N_x$, x=0.2 due to the creation of π-π interactions between N ions and the nearest O ions of ZrO_2 experience fewer atom displacements than t-ZrO_{2-x}, x=0.2 [42]. Therefore, the intensity of shear strain is lower than that of t-ZrO_{2-x}, x=0.2, which leads to lower plastic deformations. The t-ZrO_{2-x}, x=0.2 exhibits a scattered deformation map for shear strain compared to perfect and t-$ZrO_{2-x}N_x$, x=0.2. In other words, t-ZrO_{2-x}, x=0.2 undergoes more plastic deformation as it exhibits the highest magnitude of atomic displacement. Therefore, the plastic deformation zone shape of the t-ZrO_{2-x}, x=0.2 is larger than the other ones. It seems that, In comparison to N-dopants, vacancy defects exhibit a remarkable ability to serve as efficient pathways for the rapid transfer of energy from the applied indentation force away from the indenter. This efficient transfer facilitates the deformation and stress distribution around the indenter, ultimately assisting in the movement of cracks.

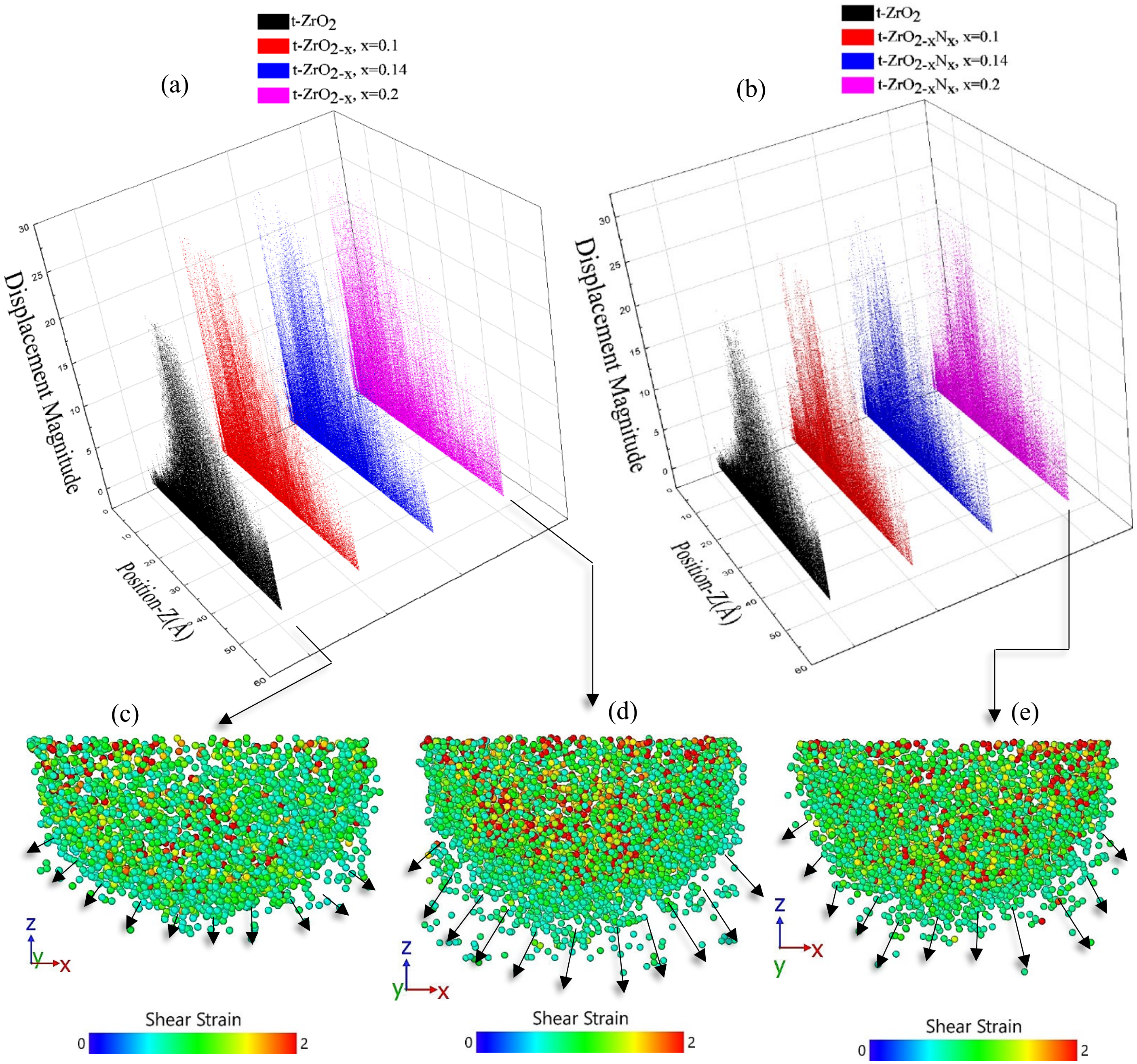

Fig. 8. (a) Comparison of the distributions of atomic displacements along the z direction of the perfect t-ZrO_2 with t-ZrO_{2-x}, x = 0.1, 0.14, and 0.2 (b) the perfect t-ZrO_2 with t-$ZrO_{2-x}N_x$, x = 0.1, 0.14, and 0.2 (c) colored deformation map of the perfect t-ZrO_2, (d) colored deformation map of

$t\text{-}ZrO_{2\text{-}x}$, x =0.2, and (e) colored deformation map of $t\text{-}ZrO_{2\text{-}x}N_x$, x =0.2. Note: Atoms experiencing shear strains below 0.5 under the indenter have been removed.

3.3.1 The Griffith energy balance concept

Indentation energies, such as the energy release rate (G_{in}) and the free energy needed for plastic deformation, are crucial parameters for studying the deformation behavior of materials. The value of G_{in} relates to plastic deformation, fracture, and delamination around the indenter. It represents the reduction in total potential energy with an increase in deformation surface area. Additionally, accurately assessing the deformation behavior needs estimating the free energy required for plastic deformation and the strain energy stored in the elastic medium. In order to obtain more precise values of G_{in}, we applied the methodology suggested in ref [76] which is based on the energy approach analysis; deformation and delamination growth of materials is governed by the net energy of a static crack, which is defined as in Eq 4.

$$U = -U_e + U_s + W_d \tag{4}$$

Where U_e and U_s are the strain energy stored in the elastic medium, and the free energy needed for deformation, respectively. In addition, W_d is known as the external mechanical work done by the sphere indenter. To achieve the thermodynamic equilibrium by balancing the three mentioned energies, it should be stated that:

$$U = 0 \tag{5}$$

Therefore, the free energy desired at the area of the deformed surface would be attained by rearranging Eq. (6) as follows:

$$U_s = U_e - W_d \tag{6}$$

The calculation of U_e and W_d from the dual cyclic nanoindentation test is comprehensively explained and illustrated in Fig. S6. Finally, the energy release rate is calculated as follows [77]:

$$G_{in} = \frac{U_s}{A} = \frac{U_e - W_d}{\pi r_i^2} \tag{7}$$

Where A represents the delamination or deformation area, which is defined in Fig. S4. The free energy required for plastic deformation, strain energy in the elastic medium, and energy release rate of perfect t-ZrO_2, t-ZrO_{2-x}, and t-$ZrO_{2-x}N_x$ at the maximum indentation depth are summarized in Table S2. Additionally, Fig. 9 presents a comparison of the values of U_s and G_{in} among perfect t-ZrO_2, t-ZrO_{2-x}, and t-$ZrO_{2-x}N_x$ at different defect concentrations. The depicted results reveal that the calculated free energy value for t-ZrO_{2-x} with a defect concentration of x=0.1 is 783.23 nJ, significantly lower than the value of 1431 nJ observed for perfect t-ZrO_2. The data for the t-$ZrO_{2-x}N_x$, x=0.1 is in between these values (1147.79nJ). As a result, perfect t-ZrO_2 exhibits the highest needed free energy for plastic deformation during cyclic nanoindentation. This finding is linked to the resistance of perfect t-ZrO_2 towards plastic deformation, which is in line with its lowest $E_{plastic}$ value (Table 3). Furthermore, as depicted in Fig. 9, the U_s values demonstrate a lower magnitude for t-ZrO_{2-x} in contrast to t-$ZrO_{2-x}N_x$. As well as it increases with increasing defect concentrations. Based on these findings, it can be inferred that among the defective structures, t-ZrO_{2-x}, x=0.1 exhibits the lowest free energy value, while t-$ZrO_{2-x}N_x$,x=0.2 displays the highest value. These results indicate that t-ZrO_{2-x}, x=0.1 experiences the most pronounced level of spontaneous plastic deformation, whereas t-$ZrO_{2-x}N_x$,x=0.2 demonstrates minimal levels of such deformation. Consequently, reaching the same nanoindentation depth requires the highest thermodynamic work for t-ZrO_{2-x}, x=0.1, and the lowest for t-$ZrO_{2-x}N_x$, x=0.2 respectively (Table S2).

Intriguingly, the value of G_{in} decreases upon the introduction of point defects into the perfect t-ZrO_2 crystal, as evidenced by Fig. 9. Significant decreases of 45.47% and 17.15% are observed in the value of G_{in} in perfect t-ZrO_2 upon introducing 0.1 of OV and N-dopants, respectively. Besides, the G_{in} value of t-ZrO_{2-x} is ca. 1.50 times lower than that of t-$ZrO_{2-x}N_x$. The observed trends in G_{in} values for the three N-dopant concentrations (x=0.2 > x=0.14 > x=0.1) exhibit distinct similarities to oxygen-deficient t-ZrO_{2-x} samples. The dependence of G_{in} on the presence of defects is attributed to the formation of major residual indentation stresses in the t-ZrO_2 under nanoindentation; such stresses tend to decrease the energy release rate and hence lead to the larger value of the apparent G_{in}. Thus, the reduced G_{in} of t-ZrO_{2-x} is attributed to enhanced plastic deformation and shear strain towards the vacancy during the loading process, leading to increased permanent residual displacement upon load reaction.

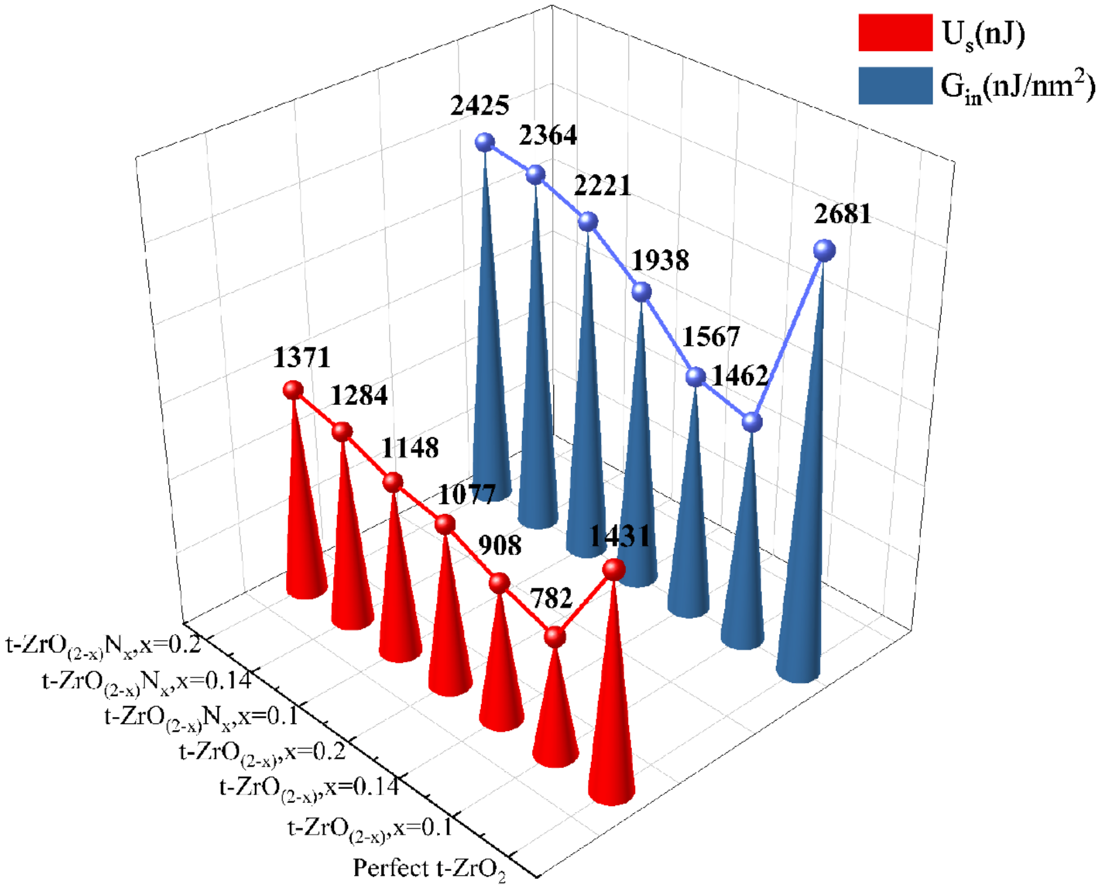

Fig. 9. Comparison of the values of U_s and G_{in} among perfect t-ZrO_2, t-ZrO_{2-x}, and t-$ZrO_{2-x}N_x$ at different defect concentrations

Additionally, the introduction of vacancy or N-dopant defects into the t-ZrO_2 crystal reveals a positive impact on the strain energy stored in the elastic medium. The value of U_e decreases in the order of t-ZrO_{2-x} > t-$ZrO_{2-x}N_x$ > perfect-ZrO_2 (Table S2). This trend is contrary to the variation of U_s. Likewise, ca. 0.45% and ca. 0.79% increases of U_e is witnessed for t-ZrO_{2-x} and t-$ZrO_{2-x}N_x$ by changing the OV or N-dopant concentration from x=0.1 to x=0.14, respectively. It is worth noting that the strain energy stored in the elastic medium is directly linked to plastic deformation and the increased shear strain. As we discussed in section 3.2.2, the t-ZrO_{2-x}, x=0.2 exhibits the highest shear strain at the maximum indentation depth. This phenomenon suggests that the presence of vacancy defects increases dislocation density, resulting in higher strain energy stored in the elastic medium of t-ZrO_{2-x} compared to t-$ZrO_{2-x}N_x$.

4. Conclusion

In summary, motivated by the promising applications of defective t-ZrO_2, we performed First-principle calculations to explore how oxygen vacancies and N-dopants affect the structural and electronic properties of t-ZrO_2. Furthermore, we compared the tunable plasticity of t-ZrO_{2-x} and t-$ZrO_{2-x}N_x$ at different defect concentrations (x = 0.1, 0.14, and 0.2), focusing on the energy release rate and free energy needed for plastic deformation during cyclic nanoindentation simulations. Our findings demonstrated that vacancy defects and N-dopants induce long-range and short-range atomic displacements in the t-ZrO_2 crystal, respectively. As a result, they enabled the tuning and modification of the structural, electronic properties, and plasticity of wide band gap t-ZrO_2. The band gap energies of defective structures exhibited a substantial reduction, ranging from 2.5 eV to 1.28 eV for t-ZrO_{2-x}, (x=0.1 to 0.2) and from 3.74 eV to 3.49 eV for t-$ZrO_{2-x}N_x$, (x=0.1 to 0.2). This noteworthy decrease is compared to the perfect structure's band gap of 5.6 eV. Furthermore, extensive discussions were provided to analyze the impact of vacancy and N-dopant defects on tuning the plasticity of t-ZrO_2 through energy-based nanoindentation analysis. MD simulations showed that the plastic deformation zone pattern and energy release rate in -ZrO_2 beneath the indenter were predominantly influenced by oxygen vacancy defects, rather than N-dopants. In conclusion, t-ZrO_{2-x}, x=0.1 demonstrated substantial spontaneous plastic deformation, whereas t-$ZrO_{2-x}N_x$,x=0.2 exhibited minimal levels of such deformation. Overall, the study is crucial to establish a solid understanding of tuning the plasticity and electronic properties of t-ZrO_2 through defect engineering. This knowledge makes defective t-ZrO_2 highly intriguing for future investigations and emerging technological applications with precisely tailored properties.

Conflicts of interest

The authors declare that they have no known competing financial interests or personal relationships that could have appeared to influence the work reported in this paper.

Acknowledgements

This work has been funded by the French National Research Agency (ANR) through the InnOxiCat project ANR-20-CE05-0010.

References

[1] Lichchhavi, A. Kanwade, P.M. Shirage, A review on synergy of transition metal oxide nanostructured materials: Effective and coherent choice for supercapacitor electrodes, J. Energy Storage. 55 (2022) 105692. https://doi.org/https://doi.org/10.1016/j.est.2022.105692.

[2] S.-H. Guan, X.-J. Zhang, Z.-P. Liu, Energy Landscape of Zirconia Phase Transitions, J. Am. Chem. Soc. 137 (2015) 8010–8013. https://doi.org/10.1021/jacs.5b04528.

[3] N.-W. Lee, K.R. Yoon, J.-Y. Lee, Y. Park, S.-J. Pyo, G.-Y. Kim, D.-H. Ha, W.-H. Ryu, Highly Conductive Off-Stoichiometric Zirconium Oxide Nanofibers with Controllable Crystalline Structures and Bandgaps and Improved Electrochemical Activities, ACS Appl. Energy Mater. 2 (2019) 3513–3522. https://doi.org/10.1021/acsaem.9b00283.

[4] L. Akhkozov, I. Danilenko, V. Podhurska, A. Shylo, B. Vasyliv, O. Ostash, A. Lyubchyk,

Zirconia-based materials in alternative energy devices - A strategy for improving material properties by optimizing the characteristics of initial powders, Int. J. Hydrogen Energy. 47 (2022) 41359–41371. https://doi.org/https://doi.org/10.1016/j.ijhydene.2021.11.193.

[5] H. Aydın, U. Kurtan, M. Demir, S. Karakuş, Synthesis and Application of a Self-Standing Zirconia-Based Carbon Nanofiber in a Supercapacitor, Energy & Fuels. 36 (2022) 2212–2219. https://doi.org/10.1021/acs.energyfuels.1c04208.

[6] Y. Wang, Y. Zhang, H. Lu, Y. Chen, Z. Liu, S. Su, Y. Xue, J. Yao, H. Zeng, Novel N-doped ZrO(2) with enhanced visible-light photocatalytic activity for hydrogen production and degradation of organic dyes., RSC Adv. 8 (2018) 6752–6758. https://doi.org/10.1039/c7ra12938f.

[7] M. Ali, E. Pervaiz, U. Sikandar, Y. Khan, A review on the recent developments in zirconium and carbon-based catalysts for photoelectrochemical water-splitting, Int. J. Hydrogen Energy. 46 (2021) 18257–18283. https://doi.org/10.1016/j.ijhydene.2021.02.202

[8] R. Gao, J. Zhu, D. Yan, Transition metal-based layered double hydroxides for photo (electro) chemical water splitting: a mini review, Nanoscale. 13 (2021) 13593–13603. https://doi.org/10.1039/D1NR03409J

[9] Y. Okamoto, First-principles molecular dynamics simulation of O2 reduction on ZrO2 (1¯ 1 1) surface, Appl. Surf. Sci. 255 (2008) 3434–3441. https://doi.org/https://doi.org/10.1016/j.apsusc.2008.09.061.

[10] K.A. Zemski, D.R. Justes, A.W. Castleman, Studies of Metal Oxide Clusters: Elucidating Reactive Sites Responsible for the Activity of Transition Metal Oxide Catalysts, J. Phys. Chem. B. 106 (2002) 6136–6148. https://doi.org/10.1021/jp0142334.

[11] J. Pan, X.L. Tian, S. Zaman, Z. Dong, H. Liu, H.S. Park, B.Y. Xia, Recent progress on transition metal oxides as bifunctional catalysts for lithium-air and zinc-air batteries, Batter. Supercaps. 2 (2019) 336–347. https://doi.org/10.1002/batt.201800082

[12] Y. Wang, J. Li, Z. Wei, Transition-metal-oxide-based catalysts for the oxygen reduction reaction, J. Mater. Chem. A. 6 (2018) 8194–8209. https://doi.org/10.1039/C8TA01321G

[13] A. Tyagi, S. Banerjee, J. Cherusseri, K.K. Kar, Characteristics of transition metal oxides, Handb. Nanocomposite Supercapacitor Mater. I Charact. (2020) 91–123.

[14] H. Li, S. Kelly, D. Guevarra, Z. Wang, Y. Wang, J.A. Haber, M. Anand, G.T.K.K. Gunasooriya, C.S. Abraham, S. Vijay, Analysis of the limitations in the oxygen reduction activity of transition metal oxide surfaces, Nat. Catal. 4 (2021) 463–468.

[15] Y. Ma, X. Xie, W. Yang, Z. Yu, X. Sun, Y. Zhang, X. Yang, H. Kimura, C. Hou, Z. Guo, W. Du, Recent advances in transition metal oxides with different dimensions as electrodes for high-performance supercapacitors, Adv. Compos. Hybrid Mater. 4 (2021) 906–924. https://doi.org/10.1007/s42114-021-00358-2.

[16] J.Y. Kwon, J.K. Jeong, Recent progress in high performance and reliable n-type transition metal oxide-based thin film transistors, Semicond. Sci. Technol. 30 (2015) 24002. 10.1088/0268-1242/30/2/024002

[17] T. Cai, J.H. Cho, B.W. Sheldon, Mechanical Behavior of Transition Metal Oxide-Based Battery Materials, Transit. Met. Oxides Electrochem. Energy Storage. (2022) 273–298. https://doi.org/10.1002/9783527817252.ch11

[18] W. Deng, X. Ji, Q. Chen, C.E. Banks, Electrochemical capacitors utilising transition metal

oxides: an update of recent developments, Rsc Adv. 1 (2011) 1171–1178. https://doi.org/10.1039/C1RA00664A

[19] P. Kalita, S. Saini, P. Rajput, S.N. Jha, D. Bhattacharyya, S. Ojha, D.K. Avasthi, S. Bhattacharya, S. Ghosh, Oxygen vacancy mediated cubic phase stabilization at room temperature in pure nano-crystalline zirconia films: a combined experimental and first-principles based investigation, Phys. Chem. Chem. Phys. 21 (2019) 22482–22490. https://doi.org/10.1039/C9CP02121C

[20] A.R. Puigdollers, F. Illas, G. Pacchioni, Structure and properties of zirconia nanoparticles from density functional theory calculations, J. Phys. Chem. C. 120 (2016) 4392–4402. https://doi.org/10.1021/acs.jpcc.5b12185

[21] Y. Cong, B. Li, S. Yue, D. Fan, X. Wang, Effect of oxygen vacancy on phase transition and photoluminescence properties of nanocrystalline zirconia synthesized by the one-pot reaction, J. Phys. Chem. C. 113 (2009) 13974–13978. https://doi.org/10.1021/jp8103497

[22] R.A. Bapat, H.J. Yang, T. V Chaubal, S. Dharmadhikari, A.M. Abdulla, S. Arora, S. Rawal, P. Kesharwani, Review on synthesis, properties and multifarious therapeutic applications of nanostructured zirconia in dentistry, RSC Adv. 12 (2022) 12773–12793. https://doi.org/10.1039/D2RA00006G

[23] L. Shi, K.-C. Tin, N.-B. Wong, Thermal stability of zirconia membranes, J. Mater. Sci. 34 (1999) 3367–3374. https://doi.org/10.1023/A:1004681015331

[24] J. Xie, Z. Zhu, H. Tao, S. Zhou, Z. Liang, Z. Li, R. Yao, Y. Wang, H. Ning, J. Peng, Research progress of high dielectric constant zirconia-based materials for gate dielectric application, Coatings. 10 (2020) 698. https://doi.org/10.3390/coatings10070698

[25] J. Houska, J. Rezek, R. Cerstvy, Dependence of the ZrO2 growth on the crystal orientation: growth simulations and magnetron sputtering, Appl. Surf. Sci. 572 (2022) 151422. https://doi.org/https://doi.org/10.1016/j.apsusc.2021.151422.

[26] G. Liu, H.M. Zhang, M.R. Wang, H.X. Zhong, J. Chen, Preparation, characterization of ZrOxNy/C and its application in PEMFC as an electrocatalyst for oxygen reduction, J. Power Sources. 172 (2007) 503–510. https://doi.org/10.1016/j.jpowsour.2007.07.067

[27] Y. Maekawa, A. Ishihara, J.-H. Kim, S. Mitsushima, K. Ota, Catalytic activity of zirconium oxynitride prepared by reactive sputtering for ORR in sulfuric acid, Electrochem. Solid-State Lett. 11 (2008) B109. 10.1149/1.2916441

[28] A. Samanta, A theoretical study of the stability of anionic defects in cubic ZrO 2 at extreme conditions, J. Mater. Sci. 51 (2016) 4845–4855. https://doi.org/10.1007/s10853-016-9788-8

[29] N. Kumari, S. Sareen, M. Verma, S. Sharma, A. Sharma, H.S. Sohal, S.K. Mehta, J. Park, V. Mutreja, Zirconia-based nanomaterials: recent developments in synthesis and applications, Nanoscale Adv. (2022). https://doi.org/10.1039/D2NA00367H

[30] L. Wang, B. Ma, X. Ren, C. Yu, J. Tian, C. Liu, C. Deng, C. Hu, Z. Liu, J. Yu, Z. Jiang, Phase-engineering strategy of ZrO2 for enhancing the mechanical properties of porous cordierite ceramics, Mater. Today Commun. 30 (2022) 103032. https://doi.org/https://doi.org/10.1016/j.mtcomm.2021.103032.

[31] H. Jiang, R.I. Gomez-Abal, P. Rinke, M. Scheffler, Electronic band structure of zirconia and hafnia polymorphs from the GW perspective, Phys. Rev. B. 81 (2010) 85119. https://doi.org/10.1103/PhysRevB.81.085119.

[32] C.V. Reddy, B. Babu, I.N. Reddy, J. Shim, Synthesis and characterization of pure tetragonal ZrO2 nanoparticles with enhanced photocatalytic activity, Ceram. Int. 44 (2018) 6940–6948. 10.1016/j.ceramint.2018.01.123

[33] G. Liao, X. Tao, B. Fang, An innovative synthesis strategy for high-efficiency and defects-switchable-hydrogenated TiO2 photocatalysts, Matter. 5 (2022) 377–379. https://doi.org/https://doi.org/10.1016/j.matt.2022.01.006.

[34] N. Zhang, M. Asle Zaeem, Effects of twin boundaries and pre-existing defects on mechanical properties and deformation mechanisms of yttria-stabilized tetragonal zirconia, J. Eur. Ceram. Soc. 40 (2020) 108–114. https://doi.org/https://doi.org/10.1016/j.jeurceramsoc.2019.09.017.

[35] R. Devanathan, W.J. Weber, S.C. Singhal, J.D. Gale, Computer simulation of defects and oxygen transport in yttria-stabilized zirconia, Solid State Ionics. 177 (2006) 1251–1258. https://doi.org/10.1016/j.ssi.2006.06.030

[36] A. Bogicevic, C. Wolverton, Nature and strength of defect interactions in cubic stabilized zirconia, Phys. Rev. B. 67 (2003) 24106. https://doi.org/10.1103/PhysRevB.67.024106.

[37] F. Zhang, M. Batuk, J. Hadermann, G. Manfredi, A. Mariën, K. Vanmeensel, M. Inokoshi, B. Van Meerbeek, I. Naert, J. Vleugels, Effect of cation dopant radius on the hydrothermal stability of tetragonal zirconia: grain boundary segregation and oxygen vacancy annihilation, Acta Mater. 106 (2016) 48–58. https://doi.org/10.1016/j.actamat.2015.12.051

[38] A. Sinhamahapatra, J.-P. Jeon, J. Kang, B. Han, J.-S. Yu, Oxygen-deficient zirconia (ZrO2−x): a new material for solar light absorption, Sci. Rep. 6 (2016) 1–8. 10.1038/srep27218.

[39] E.-S.R. Khattab, S.S. Abd El Rehim, W.M.I. Hassan, T.S. El-Shazly, Band Structure Engineering and Optical Properties of Pristine and Doped Monoclinic Zirconia (m-ZrO2): Density Functional Theory Theoretical Prospective, ACS Omega. 6 (2021) 30061–30068. doi.org/10.1021/acsomega.1c04756

[40] B. Liu, H. Xiao, Y. Zhang, D.S. Aidhy, W.J. Weber, Investigation of oxygen point defects in cubic ZrO2 by density functional theory, Comput. Mater. Sci. 92 (2014) 22–27. https://doi.org/10.1016/j.commatsci.2014.05.017

[41] P.K. Gupta, Z.H. Khan, P.R. Solanki, Effect of nitrogen doping on structural and electrochemical properties of zirconia nanoparticles, Adv. Sci. Lett. 24 (2018) 867–872. https://doi.org/10.1166/asl.2018.10863

[42] E. Albanese, M. Leccese, C. Di Valentin, G. Pacchioni, Magnetic properties of nitrogen-doped ZrO2: Theoretical evidence of absence of room temperature ferromagnetism, Sci. Rep. 6 (2016) 31435. https://doi.org/10.1038/srep31435

[43] J.C. Garcia, L.M.R. Scolfaro, A.T. Lino, V.N. Freire, G.A. Farias, C.C. Silva, H.W.L. Alves, S.C.P. Rodrigues, E.F. da Silva Jr, Structural, electronic, and optical properties of Zr O 2 from ab initio calculations, J. Appl. Phys. 100 (2006) 104103. https://doi.org/10.1063/1.2386967

[44] S.A. Tolba, N.K. Allam, Computational design of novel hydrogen-doped, oxygen-deficient monoclinic zirconia with excellent optical absorption and electronic properties, Sci. Rep. 9 (2019) 10159. https://doi.org/10.1038/s41598-019-46778-5

[45] N. Kaiser, Y.-J. Song, T. Vogel, E. Piros, T. Kim, P. Schreyer, S. Petzold, R. Valentí, L. Alff, Crystal and Electronic Structure of Oxygen Vacancy Stabilized Rhombohedral

Hafnium Oxide, ACS Appl. Electron. Mater. 5 (2023) 754–763. https://doi.org/10.1021/acsaelm.2c01255.

[46] S. Fabris, A.T. Paxton, M.W. Finnis, A stabilization mechanism of zirconia based on oxygen vacancies only, Acta Mater. 50 (2002) 5171–5178. https://doi.org/https://doi.org/10.1016/S1359-6454(02)00385-3.

[47] F. Yubero, C. Mansilla, F.J. Ferrer, J.P. Holgado, A.R. González-Elipe, Size and shape of supported zirconia nanoparticles determined by x-ray photoelectron spectroscopy, J. Appl. Phys. 101 (2007) 124910. https://doi.org/10.1063/1.2749482

[48] Y. Guo, J. Robertson, Oxygen vacancy defects in Ta2O5 showing long-range atomic re-arrangements, Appl. Phys. Lett. 104 (2014) 112906. https://doi.org/10.1063/1.4869553

[49] Q.H. Zuo, E.N. Harstad, F.L. Addessio, C.W. Greeff, A model for plastic deformation and phase transformations of zirconium under high-rate loading, Model. Simul. Mater. Sci. Eng. 14 (2006) 1465. 10.1088/0965-0393/14/8/012

[50] J.A. Lefever, J.P. Mulderrig, J.L. Hor, D. Lee, R.W. Carpick, Disordered nanoparticle packings under local stress exhibit avalanche-like, environmentally dependent plastic deformation, Nano Lett. 18 (2018) 5418–5425. https://doi.org/10.1021/acs.nanolett.8b01640

[51] S. Wang, Z. Ma, W. Zhao, W. Zhang, C. Li, S. Yang, J. Liu, Z. Guo, H. Zhao, L. Ren, Temperature-Shift-Induced Mechanical Property Evolution of Lithium-Ion Battery Separator Using Cyclic Nanoindentation, ACS Appl. Mater. Interfaces. 14 (2022) 47578–47586. https://doi.org/10.1021/acsami.2c11680

[52] S. Zhang, X. Guo, S. Yuan, Z. Jin, W.C. Tang, Insight on the structural changes of Glass-Ceramics during nanoindentation derived from Reactive Force-Field-Based molecular dynamic simulations, Appl. Surf. Sci. 571 (2022) 151375. https://doi.org/https://doi.org/10.1016/j.apsusc.2021.151375.

[53] Q. Zhou, D. Luo, D. Hua, W. Ye, S. Li, Q. Zou, Z. Chen, H. Wang, Design and characterization of metallic glass/graphene multilayer with excellent nanowear properties, Friction. 10 (2022) 1913–1926.

[54] M. Fujikane, D. Setoyama, S. Nagao, R. Nowak, S. Yamanaka, Nanoindentation examination of yttria-stabilized zirconia (YSZ) crystal, J. Alloys Compd. 431 (2007) 250–255. https://doi.org/10.1016/j.jallcom.2006.05.058

[55] A.-R. Alao, L. Yin, Loading rate effect on the mechanical behavior of zirconia in nanoindentation, Mater. Sci. Eng. A. 619 (2014) 247–255. https://doi.org/https://doi.org/10.1016/j.msea.2014.09.101.

[56] J. Malzbender, G. De With, Indentation load–displacement curve, plastic deformation, and energy, J. Mater. Res. 17 (2002) 502–511. https://doi.org/10.1557/JMR.2002.0070

[57] A. Kleinbichler, M.J. Pfeifenberger, J. Zechner, N.R. Moody, D.F. Bahr, M.J. Cordill, New Insights into Nanoindentation-Based Adhesion Testing, JOM. 69 (2017). https://doi.org/10.1007/s11837-017-2496-2.

[58] A. Kedharnath, R. Kapoor, A. Sarkar, Classical molecular dynamics simulations of the deformation of metals under uniaxial monotonic loading: A review, Comput. Struct. 254 (2021) 106614. https://doi.org/10.1016/j.compstruc.2021.106614

[59] J. Zhang, M. Zhang, L. Deng, J. Jin, P. Gong, X. Wang, Mechanical behavior of tetragonal zirconia nanopillars subjected to uniaxial loading: A molecular dynamics study, Mech. Mater. 151 (2020) 103666. https://doi.org/10.1016/j.mechmat.2020.103666

[60] D. Hua, X. Liu, W. Wang, Q. Zhou, Q. Xia, S. Li, J. Shi, H. Wang, Formation mechanism of hierarchical twins in the CoCrNi medium entropy alloy, J. Mater. Sci. Technol. 140 (2023) 19–32. https://doi.org/https://doi.org/10.1016/j.jmst.2022.08.033.

[61] J. Zhou, Z. Jiao, J. Zhang, Z. Zhong, Nanoindentation of single-crystal and polycrystalline yttria-stabilized zirconia: A comparative study by experiments and molecular dynamics simulations, J. Alloys Compd. 878 (2021) 160336. https://doi.org/10.1016/j.jallcom.2021.160336

[62] W. Kohn, L.J. Sham, Self-consistent equations including exchange and correlation effects, Phys. Rev. (1965). https://doi.org/10.1103/PhysRev.140.A1133.

[63] V. Gromov, Study of humboldtine for sodium battery anode, (2022).

[64] D. Joubert, From ultrasoft pseudopotentials to the projector augmented-wave method, Phys. Rev. B - Condens. Matter Mater. Phys. (1999). https://doi.org/10.1103/PhysRevB.59.1758.

[65] M. Monti, M. Stener, E. Coccia, Electronic circular dichroism from real-time propagation in state space, J. Chem. Phys. 158 (2023) 84102. 10.1063/5.0136392

[66] J.P. Perdew, K. Burke, M. Ernzerhof, Generalized gradient approximation made simple, Phys. Rev. Lett. (1996). https://doi.org/10.1103/PhysRevLett.77.3865.

[67] S. Plimpton, Fast parallel algorithms for short-range molecular dynamics, J. Comput. Phys. (1995). https://doi.org/10.1006/jcph.1995.1039.

[68] Z. Lu, A. Chernatynskiy, M.J. Noordhoek, S.B. Sinnott, S.R. Phillpot, Nanoindentation of ZrO2 and ZrO2/Zr systems by molecular dynamics simulation, J. Nucl. Mater. 486 (2017) 250–266. https://doi.org/10.1016/j.jnucmat.2017.01.022

[69] S.R. Phillpot, A.C. Antony, L. Shi, M.L. Fullarton, T. Liang, S.B. Sinnott, Y. Zhang, S.B. Biner, Charge Optimized Many Body (COMB) potentials for simulation of nuclear fuel and clad, Comput. Mater. Sci. 148 (2018) 231–241. https://doi.org/https://doi.org/10.1016/j.commatsci.2018.02.041.

[70] A. Stukowski, Visualization and analysis of atomistic simulation data with OVITO-the Open Visualization Tool, Model. Simul. Mater. Sci. Eng. (2010). https://doi.org/10.1088/0965-0393/18/1/015012.

[71] T. Matei, V. Tiron, R. Jijie, G. Bulai, I.L. Velicu, D. Cristea, V. Crăciun, Band-Gap Engineering of Zirconia by Nitrogen Doping in Reactive Hipims: A Step Forward in Developing Innovative Technologies for Photocatalysts Synthesis, Available SSRN 4399357. (n.d.).

[72] H. Wu, Y. Duan, K. Liu, D. Lv, L. Qin, L. Shi, G. Tang, First-principles study of phase transition and band structure of ZrO2 under pressure, J. Alloys Compd. 645 (2015) 352–357. https://doi.org/https://doi.org/10.1016/j.jallcom.2015.05.108.

[73] A. Naldoni, M. Allieta, S. Santangelo, M. Marelli, F. Fabbri, S. Cappelli, C.L. Bianchi, R. Psaro, V. Dal Santo, Effect of Nature and Location of Defects on Bandgap Narrowing in Black TiO2 Nanoparticles, J. Am. Chem. Soc. 134 (2012) 7600–7603. https://doi.org/10.1021/ja3012676.

[74] G.K. Behrh, M. Isobe, F. Massuyeau, H. Serier-Brault, E.E. Gordon, H.-J. Koo, M.-H.

Whangbo, R. Gautier, S. Jobic, Oxygen-vacancy-induced midgap states responsible for the fluorescence and the long-lasting phosphorescence of the inverse spinel Mg (Mg, Sn) O4, Chem. Mater. 29 (2017) 1069–1075. https://doi.org/10.1021/acs.chemmater.6b03906

[75] F. Yang, L. Peng, K. Okazaki, Cyclic indentation in aluminum, J. Mater. Sci. (2007). https://doi.org/10.1007/s10853-006-0480-2.

[76] H. Xie, H. Huang, Characterization of the interfacial strength of SiNx/GaAs film/substrate systems using energy balance in nanoindentation, J. Mater. Res. (2013). https://doi.org/10.1557/jmr.2013.317.

[77] A. Abdul-Baqi, E. Van der Giessen, Delamination of a strong film from a ductile substrate during indentation unloading, J. Mater. Res. (2001). https://doi.org/10.1557/JMR.2001.0195.

Supplementary Information

Atomistic insight into the defect-induced tunable plasticity and electronic properties of tetragonal zirconia

Sara Fazeli[1*], Pascal Brault[1*], Amaël Caillard[1], Anne-Lise Thomann[1], Eric Millon[1], Soumya Atmane[1], Christophe Coutanceau[2]

[1] GREMI, Université d'Orléans / CNRS, 14 rue d'Issoudun BP6744, 45067 Orléans Cedex 2, France

[2] IC2MP, Université de Poitiers / CNRS, 4 rue Michel Brunet, 86022 Poitiers, France

Seyedehsara.fazeli@univ-orleans.fr ; Pascal.brault@ univ-orleans.fr

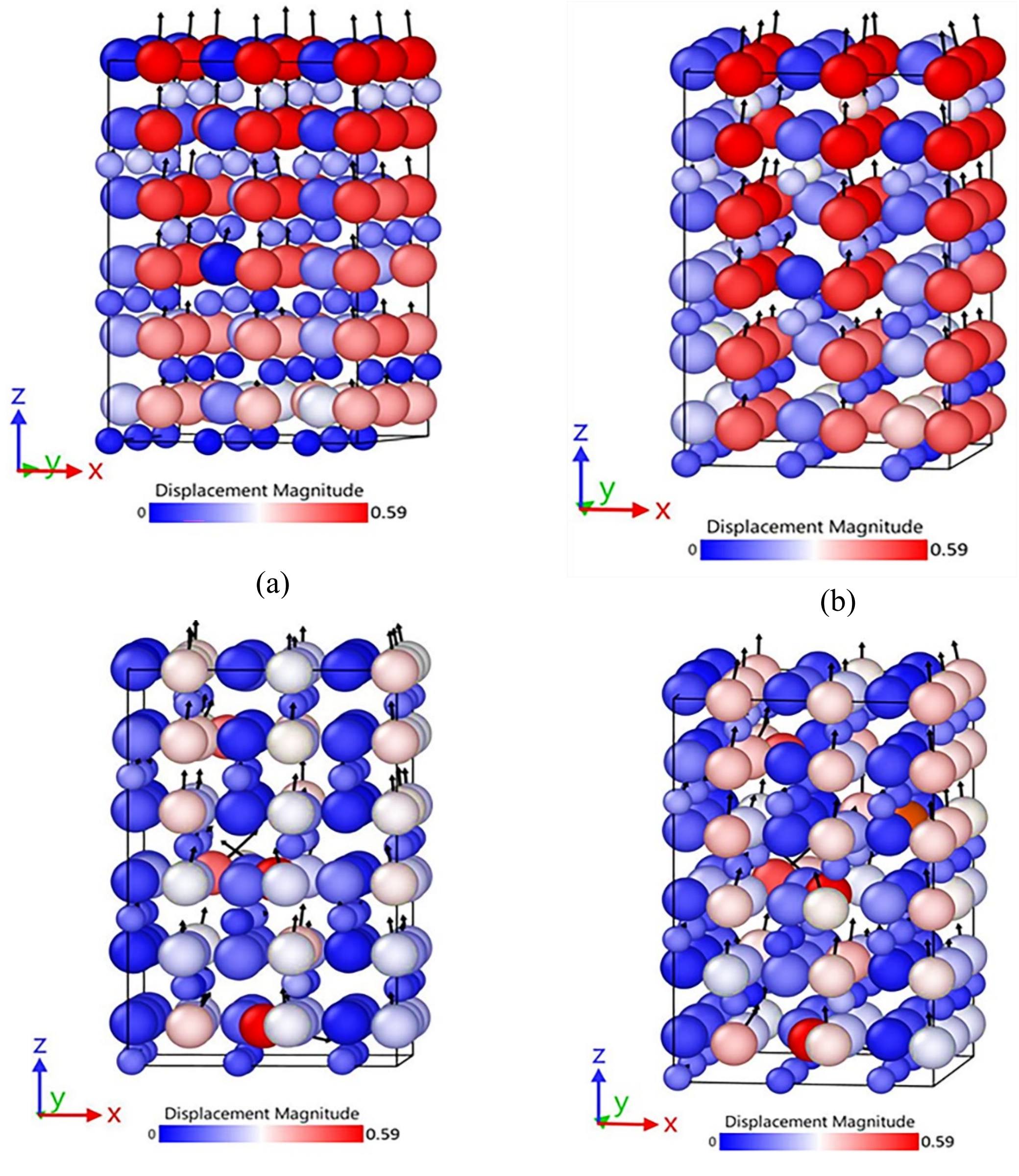

(a)

(b)

(c)

(d)

Fig. S1 (a) The magnitude of atom displacement of t-ZrO_{2-x}, x=0.14, (b t-ZrO_{2-x}, x=0.2, (c) t-ZrO $_{2-x}N_x$, x=0.14, (d) t-ZrO $_{2-x}N_x$, x=0.2

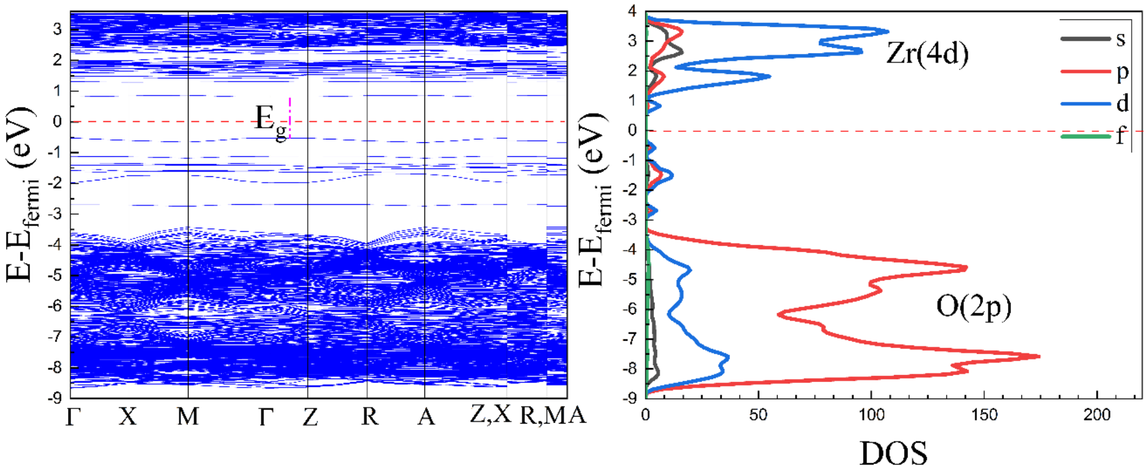
E-E$_{fermi}$ (eV)
3
2
1
0
-1
-2
-3
-4
-5
-6
-7
-8
-9
E$_g$
Γ
X
M
Γ
Z
R
A
Z,X
R,M
A
E-E$_{fermi}$ (eV)
4
3
2
1
0
-1
-2
-3
-4
-5
-6
-7
-8
-9
Zr(4d)
O(2p)
s
p
d
f
0
50
100
150
200
DOS

(a)

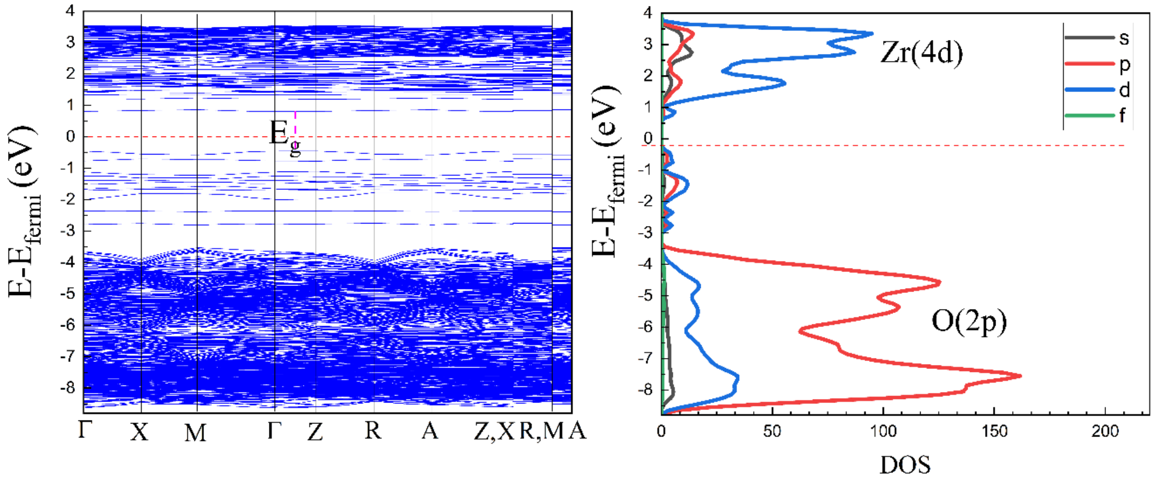
E-E$_{fermi}$ (eV)
4
3
2
1
0
-1
-2
-3
-4
-5
-6
-7
-8
E$_g$
Γ
X
M
Γ
Z
R
A
Z,X
R,M
A
E-E$_{fermi}$ (eV)
4
3
2
1
0
-1
-2
-3
-4
-5
-6
-7
-8
Zr(4d)
O(2p)
s
p
d
f
0
50
100
150
200
DOS

(b)

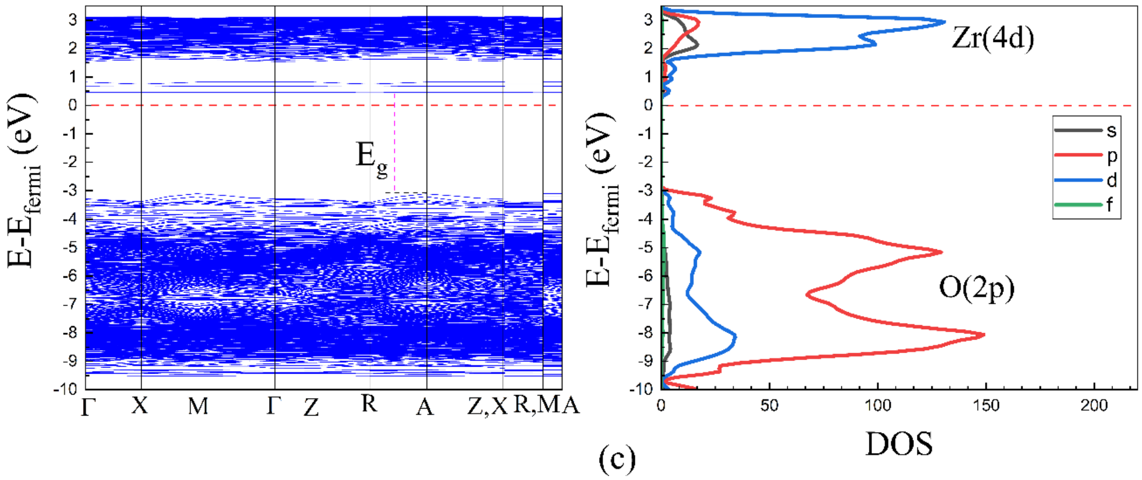

(c)

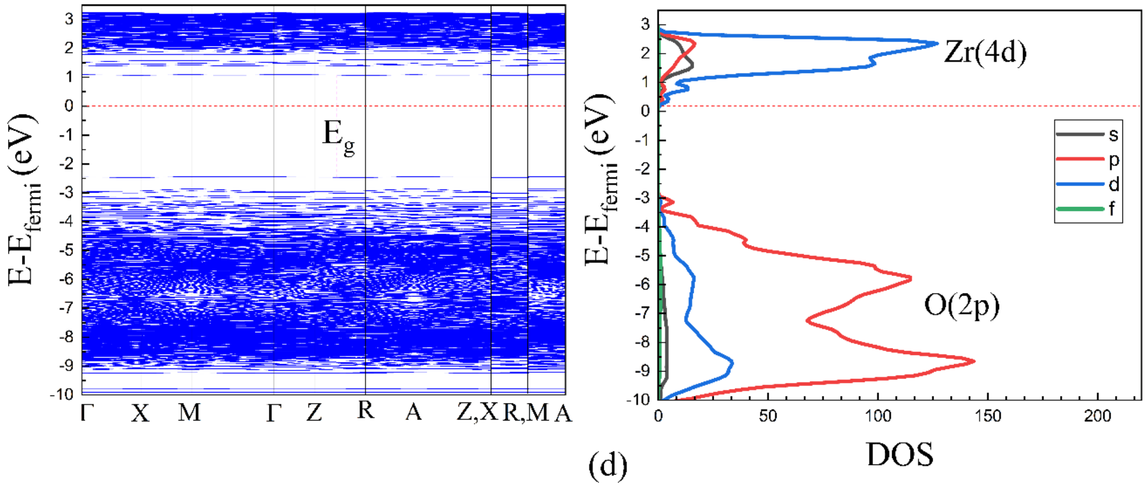

(d)

Fig. S2. band structure and DOS of (a) t- ZrO_{2-x}, x=0.14, (b) t- ZrO_{2-x}, x=0.2, (c) t- $ZrO_{2-x}N_x$, x=0.14, (d) t-$ZrO_{2-x}N_x$, x=0.2

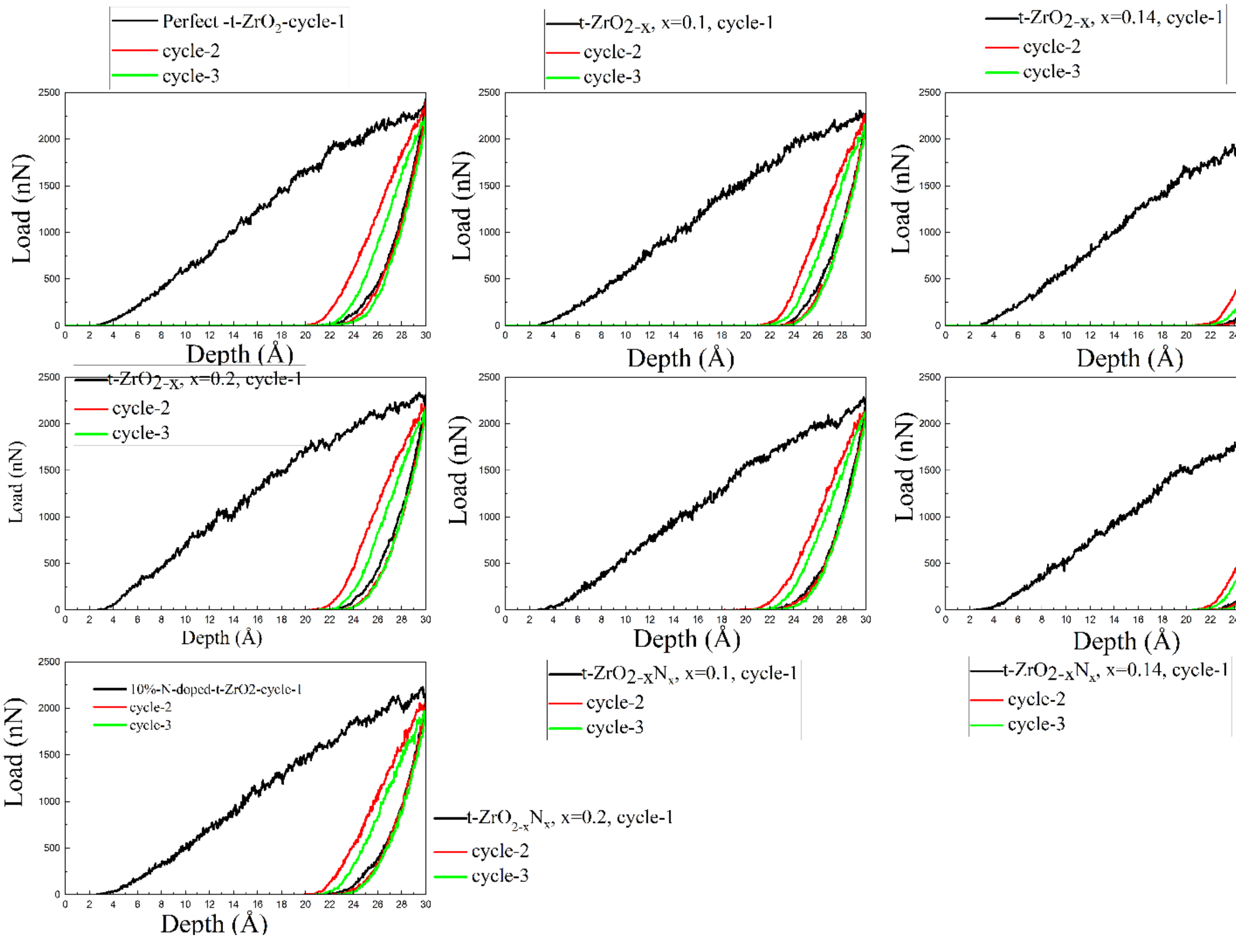

Fig. S3. Cyclic nanoindentation load-depth curves of pure and t-ZrO$_{2-x}$, x= 0.1, 0.14, and 0.2, and t-ZrO$_{2-x}$N$_{x}$, x= 0.1, 0.14, and 0.2.

Dual cyclic nanoindentation

As we mentioned in the manuscript, we used the cyclic dual-nanoindentation technique to evaluate the energy release rate during plastic deformation and delamination. Fig. S4 displays how the energy used for deformation and delamination can be achieved from a load-depth curve of the dual-indentation. Curve AB is related to the loading curve of the second nanoindentation and can be considered as the response of the elastic bending of the t-ZrO_2 film. Consequently, the area beneath the curve AB (the area enclosed by ABDA), is defined as the stored elastic strain energy of the deflected film of t-ZrO_2 at the contact depth (h_c) between the indenter and t-ZrO_2 film. The mechanical work needed for nanoindentation (W_d) is calculated by integrating the unloading part, which is the area enclosed by ACDA. Therefore, according to Eq.6 in manuscript, the free energy (Us) can be computed by calculating the area enclosed by ABCA.

It is worth mentioning that h_c can be obtained from by Oliver-Pharr method as follow:

$$h_c = h_{max} - 0.72\,\frac{P_{max}}{S_{max}} \qquad \text{(S1)}$$

Where h_{max} is the maximum indentation depth, P_{max} is the force at the maximum indentation depth, and S_{max} is the contact stiffness, which is can be considered as the slope of the unloading curve at initially stage of unloading. The values of P_{max}, S_{max}, and h_c for pure-t-ZrO2, and t-$ZrO_{(2-x)}$, and t-$ZrO_{(2-x)}N_x$ are listed in Table S1.

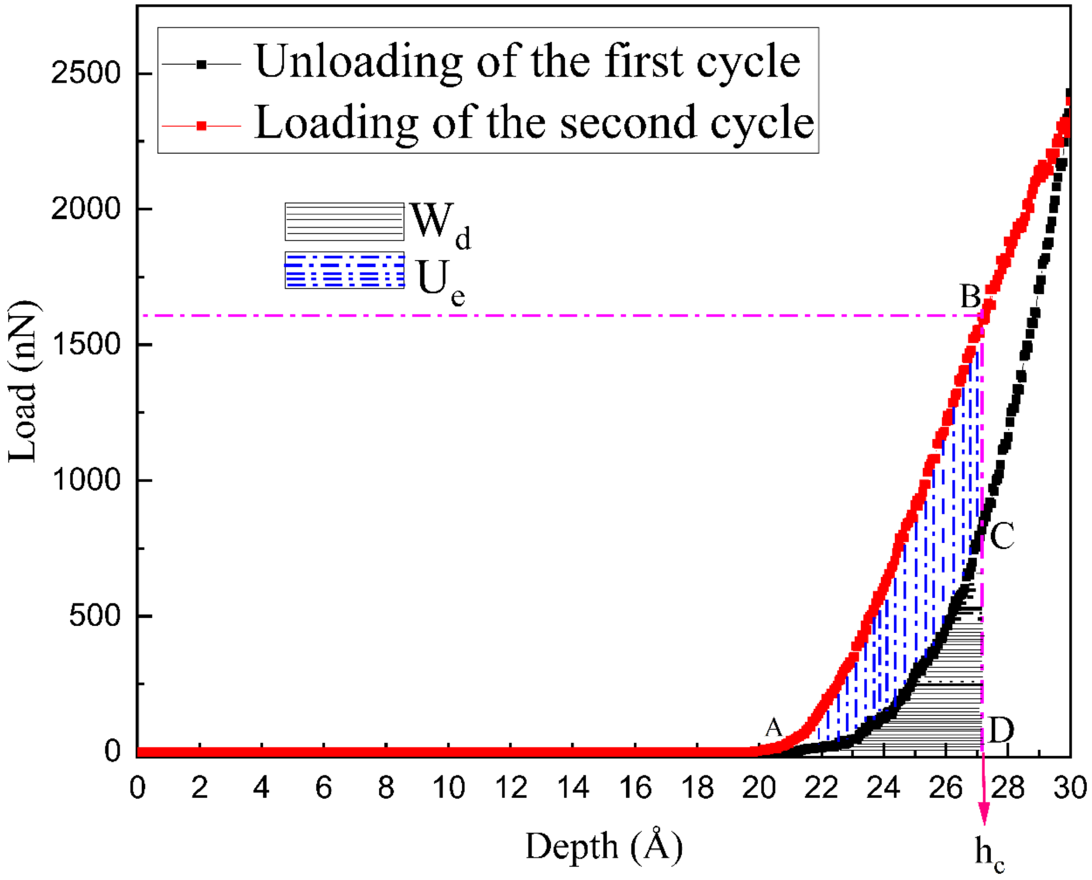

Fig. S4. Illustration of the energy calculation for indention-induced delamination.

Delamination area

In order to calculate the energy release rate, the delamination area should be calculated correctly. The measurement of the geometry of the deformation beneath the indenter and the radius of the deformation is difficult. Nevertheless, it can be estimated as a diaphragm, which clamped on a circular boundary. The radius can be approximated by evaluating the deflection of the diaphragm under a dual-indentation load. We employed the Hertz contact loaded plate model to determine the radius of crack induced via a spherical indenter, as shown in Fig. S5, the connection between a nanoindentation load and the yield deflection of the clamped diaphragm underneath a load of P is shown as:

$$h = \left(\frac{9P^2}{16RE^2}\right)^{1/3} + \frac{3Pr_c^2(1-\vartheta^2)}{4\pi Ed^3} \qquad \text{(S2)}$$

Where h, P, R, are the indentation depth, the load, and the indenter tip radius, respectively. In addition, E, d, and r_c are the elastic modulus of the film, the thickness, and the crack radius, respectively. The thickness and the Poisson's ratio of the t-ZrO_2 film is indicated as d and ν, respectively.

With the calculation of the radius, the area of delamination is computed by:

$$A = \pi r_i^2 \qquad \text{(S3)}$$

Fig

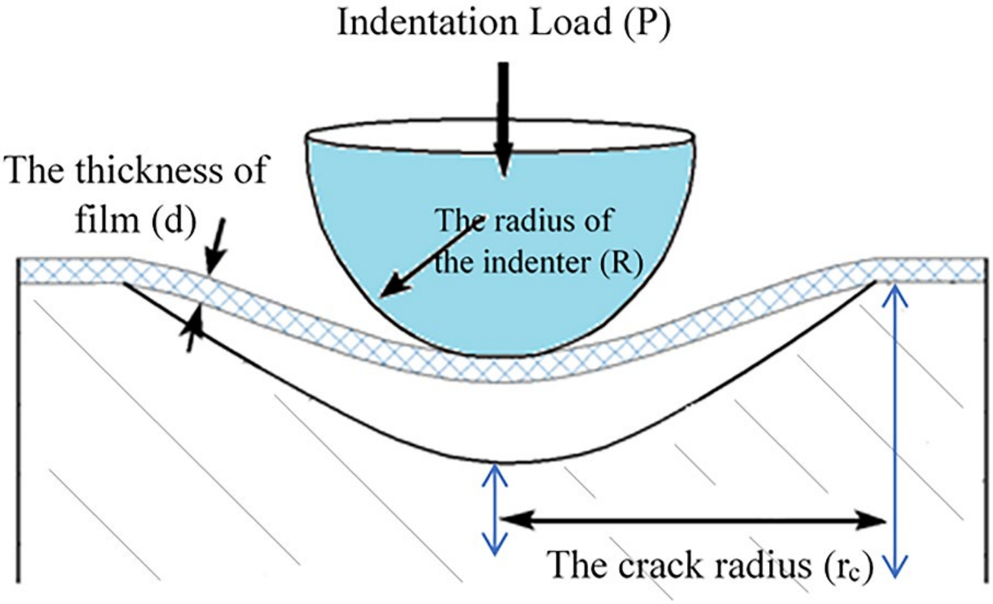

Fig. S5. The centrally loaded clamped circular plate model for delamination area estimation

Table S1. The values of P_{max}, S_{max}, and h_c for pure-t-ZrO_2, and t-ZrO_{2-x}, and t-$ZrO_{2-x}N_x$, x=0.1, 0.14, 0.2.

	P_{max}(nN)	S_{max}	h_c (Å)	r_c(Å)
Perfect t-ZrO_2	2429.17	686.94	27.45	4.12
$ZrO_{2-x},_{x=0.1}$	2277.62	646.2	27.46	4.12
$ZrO_{2-x},_{x=0.14}$	2247.18	690.33	27.65	4.29
$ZrO_{2-x},_{x=0.2}$	2289.67	674.59	27.55	4.20
$ZrO_{2-x}N_{x,\ x=0.1}$	2269.11	621.83	27.37	4.05
$ZrO_{2-x}N_{x,\ x=0.14}$	2138.17	616.26	27.50	4.15
$ZrO_{2-x}N_{x,\ x=0.2}$	2158.82	647.53	27.59	4.24

Table S2. The amounts of free energy needed for deformation (U_s), the strain energy stored in the elastic medium (U_e), the external mechanical work done by the sphere indenter (W_d), and the energy release rate of the pure t-ZrO_2, t-ZrO_{2-x}, and t-$Zr_{2-x}N_x$ x= 0.1, 0.14, and 0.2 during cyclic nanoindentation

	U_e (nJ)	W_d (nJ)	U_s (nJ)	G_{in} (nJ/nm^2)
Perfect t-ZrO_2	109	266	1431	2681
t-$ZrO_{2-x,x=0.1}$	220	142	782	1462
t-$ZrO_{2-x,x=0.14}$	228	137	908	1567
t-$ZrO_{2-x,x=0.2}$	267	160	1077	1938
t-$ZrO_{2-x}N_{x,\ x=0.1}$	126	241	1148	2221
t-$ZrO_{2-x}N_{x,\ x=0.14}$	124	253	1284	2364
t-$ZrO_{2-x}N_{x,\ x=0.2}$	149	286	1371	2425